THE JOURNAL OF BIOLOGICAL CHEMISTRY VOL. 290, NO. 49, pp. 29313–29328, December 4, 2015


# Assembly of Multi-tRNA Synthetase Complex via Heterotetrameric Glutathione Transferase-homology Domains*

Received for publication, September 9, 2015, and in revised form, October 10, 2015 Published, JBC Papers in Press, October 15, 2015, DOI 10.1074/jbc.M115.690867

**Ha Yeon Cho[‡], Seo Jin Maeng[‡], Hyo Je Cho[‡], Yoon Seo Choi[‡], Jeong Min Chung[§], Sangmin Lee[§], Hoi Kyoung Kim[¶], Jong Hyun Kim[¶], Chi-Yong Eom[‖], Yeon-Gil Kim**, Min Guo[‡‡], Hyun Suk Jung[§], Beom Sik Kang[‡1], and Sunghoon Kim[¶§§2]**

*From the [‡]School of Life Science and Biotechnology, KNU Creative BioResearch Group, Kyungpook National University, Daegu 702-701, Korea, the [§]Department of Biochemistry, College of Natural Sciences, Kangwon National University, Chuncheon 200-701, Korea, the [¶]Department of Molecular Medicine and Biopharmaceutical Sciences, Medicinal Bioconvergence Research Center, Graduate School of Convergence Technology, Seoul National University, Seoul 151-742, Korea, the [‖]NanoBio Convergence Research Team, Western Seoul Center, Korea Basic Science Institute, Seoul 120-750, Korea, the **Pohang Accelerator Laboratory, Pohang University of Science and Technology, Pohang 790-834, Korea, the [‡‡]Department of Cancer Biology, The Scripps Research Institute, Jupiter, Florida 33458, and the [§§]The National Center for Drug Screening, Shanghai Institute of Materia Medica, Shanghai 201203, China*

**Background:** GST domains have been found in diverse proteins involved in translational systems.
**Results:** Four GST domains from human methionyl-tRNA synthetase, glutaminyl-prolyl-tRNA synthetase, ARS-interacting multifunctional protein (AIMP) 2, and AIMP3 are complexed in an ordered fashion.
**Conclusion:** Four components in the human multisynthetase complex are assembled through a GST domain tetrameric complex.
**Significance:** GST domain assemblies act as scaffolds for the formation of multicomponent protein complexes.

**Many multicomponent protein complexes mediating diverse cellular processes are assembled through scaffolds with specialized protein interaction modules. The multi-tRNA synthetase complex (MSC), consisting of nine different aminoacyl-tRNA synthetases and three non-enzymatic factors (AIMP1–3), serves as a hub for many signaling pathways in addition to its role in protein synthesis. However, the assembly process and structural arrangement of the MSC components are not well understood. Here we show the heterotetrameric complex structure of the glutathione transferase (GST) domains shared among the four MSC components, methionyl-tRNA synthetase (MRS), glutaminyl-prolyl-tRNA synthetase (EPRS), AIMP2 and AIMP3. The MRS-AIMP3 and EPRS-AIMP2 using interface 1 are bridged via interface 2 of AIMP3 and EPRS to generate a unique linear complex of MRS-AIMP3:EPRS-AIMP2 at the molar ratio of (1:1):(1:1). Interestingly, the affinity at interface 2 of AIMP3:EPRS can be varied depending on the occupancy of interface 1, suggesting the dynamic nature of the linear GST tetramer. The four components are optimally arranged for maximal accommodation of additional domains and proteins. These characteristics suggest the GST tetramer as a unique and dynamic structural platform from which the MSC components are assembled. Considering prevalence of the GST-like domains, this tetramer can also provide a tool for the communication of the MSC with other GST-containing cellular factors.**

Because many cellular proteins exert and regulate their activities via diverse protein-protein interactions and macromolecular structures, it is important to identify the functional domains that are used for the assembly of proteins and to understand the process through which they are assembled. In many cellular pathways, scaffolding proteins bring together multiple signaling proteins through modules specialized for protein-protein interaction (1).

Glutathione transferase (GST) conjugates the sulfhydryl group of glutathione to xenobiotic substrates for detoxification and its homologs and isoforms have been described from bacteria to humans (2). Throughout evolution, GST structures have spread into different proteins (3), including aminoacyl-tRNA synthetases (ARSs)[3] and other translational factors (4, 5). Among ARSs, GST homologs are found in methionyl-tRNA synthetase (MRS) from yeast to human and are involved in MRS catalysis (6). Mammalian valyl-tRNA synthetase, glutaminyl-prolyl-tRNA synthetase (EPRS), the largest isoform of human cysteinyl tRNA synthetase, and glutamyl-tRNA synthetase (ERS) in some species, also contain a GST domain located in their N-terminal regions (5, 7). Although the functional impli-

* This work was supported by Global Frontier Project Grant NRF-2014M3A6A4062857 of the National Research Foundation funded by the Ministry of Science, ICT & Future Planning (MSIP) of Korea. The authors declare that they have no conflicts of interest with the contents of this article.
[1] To whom correspondence may be addressed: 80 Daehak-ro, Buk-gu, Daegu 702-701, Korea. Tel.: 82-53-950-6357; Fax: 82-53-943-2762; E-mail: bskang2@knu.ac.kr.
[2] To whom correspondence may be addressed: 1 Gwanak-ro, Gwanak-gu, Seoul 151-742, Korea, Tel.: 82-2-880-8180; Fax: 82-2-888-9122; E-mail: sungkim@snu.ac.kr.

[3] The abbreviations used are: ARS, aminoacyl-tRNA synthetases; MSC, multi-tRNA synthetase complex; MRS, methionyl-tRNA synthetase; EPRS, glutaminyl-prolyl-tRNA synthetase; AIMP, ARS-interacting multifunctional protein; MR, molecular replacement; ITC, isothermal titration calorimetry; ERS, glutamyl-tRNA synthetase; I3C, 5-amino-2,4,5-triiodoisophthalic acid; Ni-NTA, nickel-nitrilotriacetic acid.

cations of these embedded GST domains vary, they appear to play roles in protein assembly and folding.

Human multi-tRNA synthetase complex (MSC) is a macromolecular protein complex consisting of nine different ARSs and three ARS-interacting multifunctional proteins (AIMPs) (8). ARSs catalyze covalent bond formation between specific amino acids and tRNAs for protein synthesis, and AIMPs are non-enzymatic factors. The association and dissociation of MSC components is not only critical for protein synthesis but also for the control of diverse cellular signaling pathways (9). As system complexity is accreted, several different domains have been recruited at one or both ends of the ARS catalytic domains (10). These acquired domains appear to provide flexibility and efficiency not only in catalysis but also in protein synthesis and other signaling pathways. In MSC, two ARS-associated *trans*-acting factors, AIMP2 and AIMP3, also contain the inserted GST domains in addition to MRS and EPRS. However, the roles of the GST domains in catalysis and complex formation remain poorly understood.

In this work, we selected the four components of MSC containing different GST domains and determined their interactions with the crystal structures of the binary GST domain complexes and electron microscopic structures of tetrameric complexes to understand how they are assembled. Here we present the heterotetrameric GST complex as a novel dynamic molecular framework to bring MSC components together.

## Experimental Procedures

*Protein Preparation*—We cloned the full-length human *MARS* and *AIMP2* genes into pET30a, the full-length *EPRS* into pET28a, and *EEFIE1* (for AIMP3) into the pQE80L and pProEX vectors. We subcloned the genes for the GST domains of MRS ($MRS_{GST1,2}$; 1–207 and 1–224), EPRS ($EPRS_{GST1-3}$; 1–164, 1–175, and 1–196), and AIMP2 ($AIMP_{GST1,2}$; 90–320 and 111–320), the GST-ERS region of EPRS ($EPRS_{GST4}$; 1–769) and AIMP3△C5(1–169) into the expression vectors containing His tag. For $MRS_{GST}$, pET30a; for AIMP3, pQE80L, pET30a, and pProEX; for $EPRS_{GST}$, pET30a; and for $AIMP2_{GST}$, pQE80L and pET30a vectors were used. We generated the various sizes of constructs to facilitate purification and crystallization of proteins and to distinguish well the protein bends in SDS-PAGE. Mutations for pulldown assay were introduced to $MRS_{GST2}$, AIMP3, $EPRS_{GST2}$, and $AIMP2_{GST2}$ using the QuikChange site-directed mutagenesis method and confirmed by sequencing. To generate proteins without a His tag, a stop codon (TAA) was introduced at the C terminus of the protein in the pET30a vector by mutagenesis as described above.

Protein expression of the recombinant constructs in *Escherichia coli* BL21(DE3) strain was induced with 0.2 mM isopropyl 1-thio-β-D-galactopyranoside at 18 °C. His-tagged recombinant proteins were purified by affinity chromatography using a Ni-NTA column. The harvested cells were resuspended in Tris buffer (50 mM Tris-HCl, pH 8.0) and disrupted by sonication. After centrifugation, the crude extracts were loaded onto a Ni-NTA column (Qiagen) and washed with a buffer containing 300 mM NaCl and 15 mM imidazole. The proteins were eluted with a buffer containing 200 mM imidazole. AIMP3 expressed from a pProEX vector was digested by rTEV at 21 °C in the presence of 0.5 mM EDTA and 1 mM DTT, and reapplied to a Ni-NTA column after dialysis to remove the cleaved $His_6$ tag. To obtain binary complexes, harvested cells that had expressed two different proteins were mixed and purified together as described above.

*In Vitro Pulldown Assay*—Interactions between four GST domains were examined by *in vitro* pulldown assays using the Ni-NTA affinity chromatography. $EPRS_{GST2}$ and $MRS_{GST2}$ with C-terminal $His_6$-tagged and $AIMP2_{GST2}$ and AIMP3 with N-terminal $His_6$-tagged proteins were applied to the Ni-NTA column in the presence of other proteins without $His_6$ tag and washed with 50 mM Tris-HCl buffer (pH 8.0) containing 150 mM NaCl and 5 mM imidazole to avoid nonspecific binding to the Ni-NTA beads. The samples were eluted with a buffer containing 150 mM NaCl and 200 mM imidazole. The eluted proteins were subjected to 12% SDS-PAGE. To analyze the interface between the GST domains ($MRS_{GST2}$:His-AIMP3, His-AIMP3:$EPRS_{GST2}$, and $EPRS_{GST2}$:His-$AIMP2_{GST2}$), the same protocol was used with the GST domain proteins containing the indicated mutations at interfaces 1 and 2.

*Size-exclusion Chromatographic Analysis*—To confirm the molecular weight of the different protein complexes, dimeric ($MRS_{GST2}$-His:His-AIMP3, His-AIMP3:$EPRS_{GST3}$-His, and $EPRS_{GST3}$-His:$AIMP2_{GST2}$-His), trimeric ($MRS_{GST2}$-His:His-AIMP3:$EPRS_{GST3}$-His, and His-AIMP3:$EPRS_{GST3}$-His:$AIMP2_{GST2}$-His), and tetrameric complexes ($MRS_{GST2}$-His:His-AIMP3:$EPRS_{GST3}$-His:$AIMP2_{GST2}$-His and MRS-His:His-AIMP3:His-$EPRS_{GST4}$:His-$AIMP2_{GST2}$) were co-purified using Ni-NTA affinity chromatography. The purified proteins were injected onto a Superdex 75 10/300 column (dimeric complexes) and Superdex 200 10/300 column (trimeric and tetrameric complexes) (GE Healthcare) at a flow rate of 0.5 ml/min in a buffer containing 150 mM NaCl. The molecular weights of the eluted samples were calculated based on the calibration curve of standard samples.

*FRET Analysis*—We used the pair of CFP and YFP. The genes encoding AIMP2/histidyl-tRNA synthetase (HRS), AIMP3, and EPRS/MRS were inserted into the plasmids, pAmCyan1-N1 (SalI and SmaI), pAmCyan1-C1 (SalI and SmaI), and pEYFP-N1 (XhoI and BamHI), respectively. The indicated pairs of proteins were transfected into CHO-K1 cells that were cultivated in RPMI containing 10% FBS and 1% antibiotics, using Lipofectamine 3000 (Invitrogen). Cell imaging for FRET analysis was made using a confocal laser scanning microscope (Nikon, A1Rsi) with CFI Plan Apochromat VC 20X N.A. 0.75. The CFP- and YFP-tagged proteins were analyzed by excitation at 457 nm and emission at 464–499 nm, and excitation at 514 nm and emission at 525–555 nm, respectively. For FRET analysis, we defined the co-localized region of CFP- and YFP-proteins as return of intensity and FRET efficiency was determined using NIS-Elements AR 3.2 64-bit version 3.22 (Nikon imaging software).

*Crystallization and Data Collection*—Crystallization of the complex proteins was initially performed using sparse matrix screens (Hampton Research and Emerald Biostructures) and the sitting-drop vapor diffusion method at 21 °C. After optimization, the best crystals of the $MRS_{GST1}$-His:AIMP3△C5 complex were obtained under precipitant conditions of 18%

PEG3350, 0.1 M HEPES (pH 7.7) in drops where 1.2 μl of protein solution (15 mg/ml) was mixed with 1.2 μl of precipitant solution. The protein crystals were soaked overnight in the precipitant solution containing an additional 0.2 M 5-amino-2,4,5-triiodoisophthalic acid (I3C, Hampton Research) for phasing (11). The crystal was transferred to a cryo-protectant solution containing an additional 13% glycerol in the crystallization solution, prior to x-ray diffraction data collection. A single anomalous x-ray dispersion dataset for the iodine from I3C was collected at a wavelength of 0.9793 Å using a Quantum 210 CCD detector at the 7A beamline of the Pohang Accelerator Laboratory (PAL, Korea). Data were integrated and scaled with HKL2000 (12). The $MRS_{GST1}$-His:AIMP3△C5 mutant crystal belonged to space group $P22_12_1$ with dimensions $a = 43.2$ Å, $b = 71.4$ Å, $c = 116.2$ Å and contained one complex in the asymmetric unit.

AIMP3△C5-$EPRS_{GST2}$ complex crystals were grown in 1.75 M ammonium sulfate and 0.4 M sodium chloride. The crystals were flash-frozen in liquid nitrogen for data collection with the cryo-protectant solution containing 20% glycerol. Data sets for the complex were obtained at 0.9796 Å on beamline 5C at the PAL. Data were integrated and scaled with HKL2000. The crystal diffracted to 2.6 Å, and belongs to space group $P3_1$. The unit cell dimensions of the crystal were $a = 92.1$ Å, $b = 92.1$ Å, $c = 186.0$ Å, and $\gamma = 120.0°$ with four complexes in the asymmetric unit.

After optimization, the best selenomethionine crystals of the $EPRS_{GST2}$-His:$AIMP2_{GST1}$-His complex were grown in 20% PEG3350, 0.2 M potassium citrate, whereas the crystals of the native $EPRS_{GST2}$-$AIMP2_{GST1}$-His complex were grown in 24% PEG3350, 0.2 M ammonium chloride with a protein concentration of 21.4 mg/ml. Crystals were transferred to a cryo-protectant solution containing 15% glycerol added to the crystallization solution, and the x-ray diffraction data for both crystals were collected at a wavelength of 0.9796 Å at the 5C beamline of PAL. The collected data were indexed, integrated, and scaled using the HKL-2000 software package. The $EPRS_{GST2}$-His:$AIMP2_{GST1}$-His and $EPRS_{GST1}$:$AIMP2_{GST2}$-His crystals diffracted to 3.3- and 2.6-Å resolution and belonged to space group $P4_3$ with dimensions of $a = 84.3$ Å, $b = 84.3$ Å, $c = 147.3$ Å and $P2_12_12_1$ with dimensions of $a = 94.7$ Å, $b = 111.8$ Å, $c = 181.3$ Å, respectively. Each crystal contained four complexes in the asymmetric unit.

*Structure Determination*—The structure of the I3C-soaked $MRS_{GST1}$:AIMP3△C5 complex was determined by the single anomalous dispersion method, at a resolution of 1.6 Å. Four iodine atoms were identified in the asymmetric unit using SOLVE (13), and density modification and subsequent automated model building was performed with RESOLVE (14). The RESOLVE-built partial model was used as a guide to build the remainder of the protein manually into density-modified electron density maps with the program COOT (15). Refinement with isotropic displacement parameters was performed with Refmac4 (16) in the CCP4 suite (17). The $R_{work}$ and $R_{free}$ values of the refined structure were 0.186 and 0.236, respectively.

The structure of AIMP3△C5-$EPRS_{GST2}$ was determined at a resolution of 2.6 Å by molecular replacement (MR) using the crystal structures of AIMP3 from the $MRS_{GST1}$-His:AIMP3△C5 complex and the yeast $ERS_{GST}$ structure (PDB code 2HRK) as search models. Model building and structure refinement were carried out using COOT and Phenix.Refine (18), respectively. The crystal structure was determined at a final resolution of 2.6 Å with $R_{work} = 0.138$ and $R_{free} = 0.170$.

The initial structure of $EPRS_{GST}$-$AIMP2_{GST}$ was determined by MR-single anomalous dispersion using the x-ray diffraction data set from $EPRS_{GST1}$-His:$AIMP2_{GST2}$-His (SeMet) at 3.3 Å. A partial structure of $EPRS_{GST1}$ was determined by MR using Phenix.Phaser (19) with $EPRS_{GST2}$ coordinates, taken from the previously solved AIMP3-$EPRS_{GST}$ structure, used as the search model. The anomalous signal from selenium atoms was used to obtain initial phase information with Phenix.Autosol (20), and subsequently the complex structure was built using Phenix.Autobuild (21). With the partially built model of the $EPRS_{GST1}$-His:$AIMP2_{GST2}$-His complex, the $EPRS_{GST2}$:$AIMP2_{GST1}$-His structure was solved by MR at a resolution of 2.6 Å using Phenix.Phaser. The asymmetric unit contained four $EPRS_{GST2}$-$AIMP2_{GST1}$ complexes and the Matthews coefficient, $V_m$, was calculated to be 2.65 $Å^3$/Da, corresponding to a solvent content of 53.6%. Model building and structure refinement were carried out using COOT and Phenix.Refine, respectively. The crystal structure was determined at a resolution of 2.6 Å with $R_{work} = 0.189$ and $R_{free} = 0.247$.

Data collection and model statistics for the structures of the three binary complexes are summarized in Table 1. The complex structures of $MRS_{GST1}$:AIMP3△C5, AIMP3△C5-$EPRS_{GST2}$, and $EPRS_{GST2}$-$AIMP2_{GST1}$ were deposited under PDB codes 4BVX, 5BMU, and 5A34, respectively.

*Electron Microscopy*—The purified protein samples, $MRS_{GST2}$-AIMP3-$EPRS_{GST2}$-$AIMP2_{GST1}$ and MRS-AIMP3-$EPRS_{GST4}$-$AIMP2_{GST2}$, were diluted 100-fold with 50 mM Tris buffer (pH 7.5) containing 150 mM NaCl and 2 mM DTT to a final concentration of 100 nM. The treated samples (5 μl) were immediately applied to carbon-coated grids that had been glow-discharged (Harrick Plasma, Ithaca, NY) for 3 min in air. Grids were negatively stained using 1% uranyl acetate and examined in a Technai G2 Spirit Twin transmission electron microscope fitted with anti-contaminator (FEI, U.S, used instrumentation in Korea Basic Science Institute) operated at 120 kV. Images were recorded on a 4Kx4K, Ultrascan 895 CCD camera (Gatan, USA) at a magnification of 30,000 (0.36 nm/pixel)(22). Single-particle three-dimensional reconstruction was carried out using the EMAN package approach with C1 symmetry applied (23). The protein particles in the micrographs were selected semi-automatically in 100 × 100 pixel boxes, a surface area slightly larger than the actual size of particles using the program BOXER. To eliminate any variations in the density of images, the selected particle images were masked and normalized. A set of 322 and 710 boxed particles from negatively stained molecules of the $MRS_{GST2}$-AIMP3-$EPRS_{GST2}$-$AIMP2_{GST1}$ and MRS-AIMP3-$EPRS_{GST4}$-$AIMP2_{GST2}$ complexes, respectively, were classified into five classes to provide a sufficient number of the views. Chimera (24) was used for visualization and analysis of three-dimensional volumes.

*Isothermal Titration Calorimetry (ITC)*—The binding affinity between His-AIMP3 C147S and $EPRS_{GST2}$-His was mea-

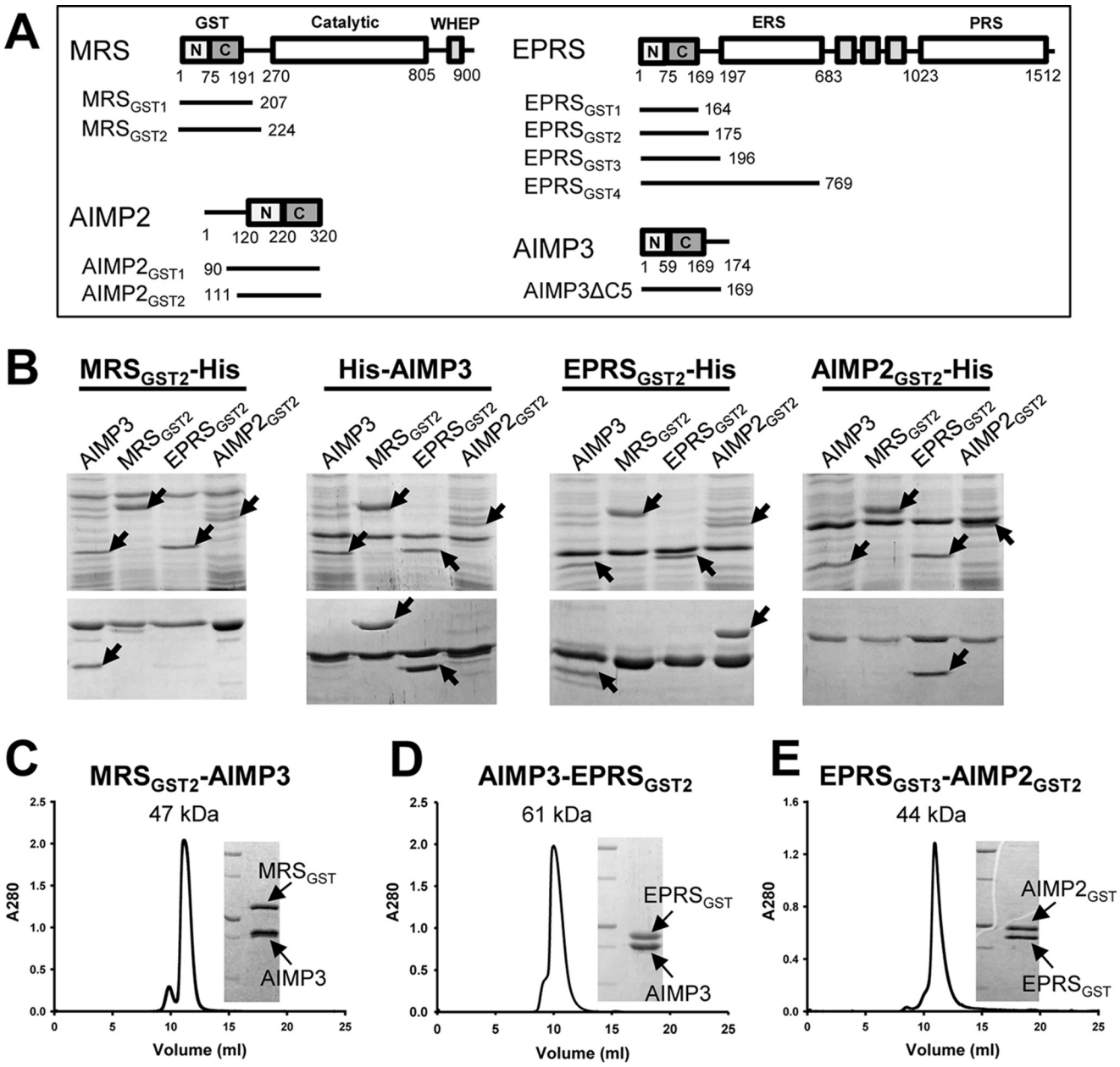


FIGURE 1. **Heterodimeric complex formation between the four GST domain proteins from the MSC.** *A*, the components of MSC, MRS, EPRS, AIMP2, and AIMP3 have a GST domain consisting of GST-N and GST-C subdomains. The different GST domain-containing peptides of the four MSC components used for this experiment are schematically represented. *B*, pairwise interactions between the different GST domains were determined by *in vitro* pulldown assays. The C-terminal His-tagged EPRS$_{GST2}$, MRS$_{GST2}$, and AIMP2$_{GST2}$ and the N-terminal His-tagged AIMP3 WT were mixed with each of the four GST domains without the His tag (*upper panels*) and purified on a Ni-NTA column (*lower panels*). Co-purified proteins were visualized by gel electrophoresis and Coomassie staining. *Arrows* indicate the untagged proteins expressed or co-purified with the indicated His-tagged protein. *C-E*, the pairs of MRS$_{GST}$-AIMP3 (*C*), AIMP3-EPRS$_{GST}$ (*D*), and EPRS$_{GST}$-AIMP2$_{GST}$ (*E*) were subjected to gel filtration chromatography. All of these pairs were eluted at the expected sizes of 1:1 heterodimeric complexes. SDS-PAGE analyses of the proteins in the elution peaks further confirmed a 1:1 heterodimer formation.

sured by the ITC method using a MicroCal iTC$_{200}$ titration calorimeter (GE Healthcare). To determine the effect of other partner proteins on the interaction of EPRS and AIMP3, complexes of MRS$_{GST2}$-His:HIS-AIMP3 C147S and EPRS$_{GST2}$-His:AIMP2$_{GST2}$-His were also used for ITC measurements. The sample cell was filled with 250 $\mu$l of EPRS$_{GST2}$-His either alone or in complex with AIMP2$_{GST2}$-His, and the syringe was filled with 40 $\mu$l of His-AIMP3 C147S either alone or in complex with MRS$_{GST2}$-His. Prior to the ITC experiment, the purified proteins were dialyzed overnight against 50 mM Tris-HCl buffer (pH 8.0) containing 150 mM NaCl and 2 mM DTT. His-AIMP3 C147S and His-AIMP3 C147S:MRS$_{GST2}$-His complex were titrated into a solution of EPRS$_{GST2}$-His and EPRS$_{GST2}$-His with AIMP2$_{GST2}$-His using the following concentrations: 331 $\mu$M His-AIMP3 C147S into 16 $\mu$M EPRS$_{GST2}$-His, 378 $\mu$M MRS$_{GST2}$-His:His-AIMP3 C147S into 14 $\mu$M EPRS$_{GST2}$-His, 346 $\mu$M His-AIMP3 C147S into 15 $\mu$M EPRS$_{GST2}$-His:AIMP2$_{GST2}$-His, 345 $\mu$M MRS$_{GST2}$-His:His-AIMP3 C147S into 15 $\mu$M EPRS$_{GST2}$-His:AIMP2$_{GST2}$-His. All experiments were conducted in 50 mM Tris buffer (pH 8.0) containing 150 mM NaCl and 2 mM DTT at 25 °C. Typically, an initial 0.4-$\mu$l injection was followed by 19 injections of 1.0 $\mu$l of syringe into the

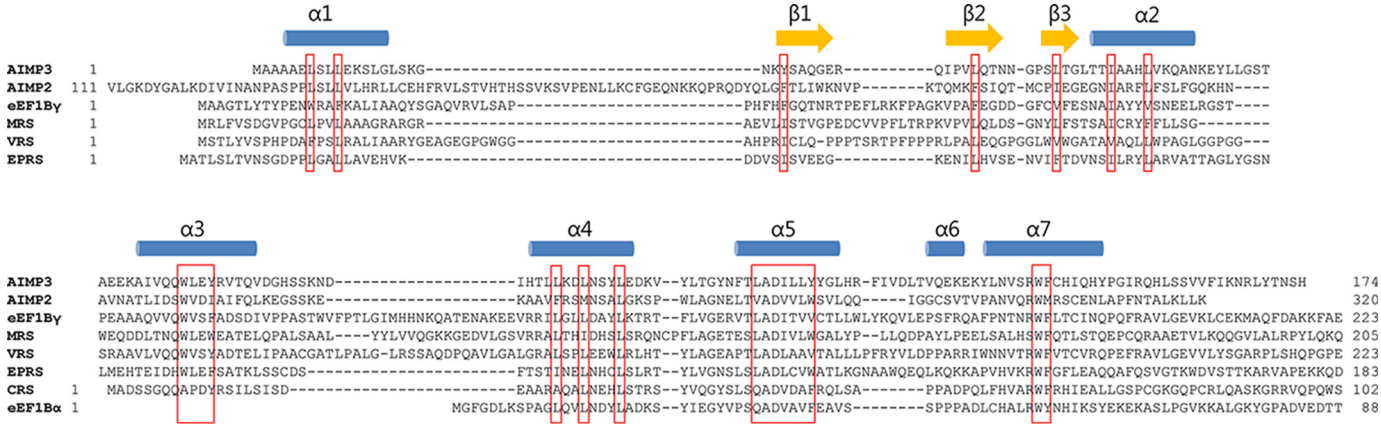


FIGURE 2. **Sequence alignment of the GST domains inserted into ARSs, AIMPs, and elongation factors.** The sequences of the GST domains were aligned pairwise using ClustalW2 (26) and manually adjusted to generate a multiple alignment. The secondary structural elements were defined based on the AIMP3 crystal structure and were marked above the sequence. *Upper* and *lower panels* are for GST-N and GST-C, respectively. The conserved residues for the GST-fold are highlighted (*red boxes*).

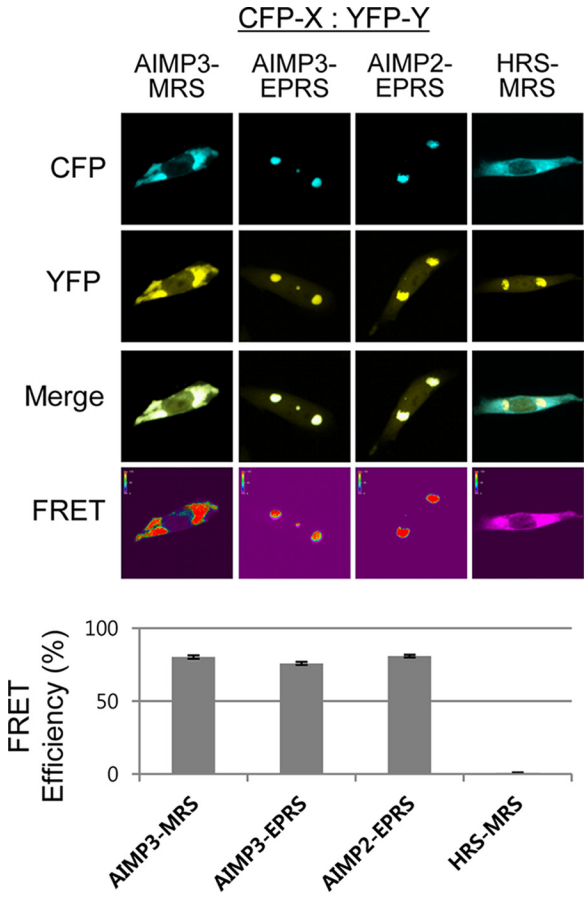


FIGURE 3. **Colocalization of the GST domain pairs *in vivo*.** Fluorescent protein (*cyan* or *yellow*) fused GST domains were expressed in CHO-K1 cells and their localization were visualized (*top*). The heterodimeric interactions between $MRS_{GST}$-AIMP3, AIMP3-$EPRS_{GST}$, and $AIMP2_{GST}$-$EPRS_{GST}$ were monitored by FRET analysis (*bottom*). The pairs of CFP-AIMP3:YFP-MRS ($n = 37$), CFP-AIMP3:YFP-EPRS ($n = 34$), CFP-AIMP2:YFP-EPRS ($n = 40$), and CFP-HRS:YFP-MRS ($n = 27$) were co-expressed in CHO-K1 cells and FRET efficiencies were measured as described under "Experimental Procedures" and represented as bar graphs.

cell constantly stirred at 1,000 rpm, and data were recorded for 150 s between injections. The heat generated from dilution was determined in separate experiments by diluting proteins into the buffer alone and was taken as the blank value for each injection. The corrected heat values were fitted using a nonlinear least squares curve-fitting algorithm (MicroCal Origin 7.0) to obtain the stoichiometry ($n$), the dissociation constant ($K_d$), and the change in enthalpy for each enzyme-ligand interaction ($\Delta H$).

## Results

*Specific Heterodimeric Interactions between GST Domains*—GST is known to be a homodimeric protein with each monomer consisting of an N-terminal thioredoxin fold (GST-N) and a C-terminal $\alpha$-helical subdomain (GST-C) (25). Among the MSC components, two ARSs (EPRS and MRS), and two AIMPs (AIMP2 and AIMP3) contain a GST domain (Fig. 1*A*). These GST domains display strong homology to the GST domain of elongation factor eEF1B$\gamma$, which belongs to the theta class (4, 5). Sequence alignment of the domains reveals that the GST-C subdomains are similar in size and well conserved in sequence, especially the residues involved in stabilizing the helical bundle structure, whereas GST-N subdomains are less conserved in size and sequence (Fig. 2).

The potential interactions between the GST domains of the four MSC components were investigated by *in vitro* pulldown assays using the His-tagged $EPRS_{GST}$, $MRS_{GST}$, and $AIMP2_{GST}$, and the full-length AIMP3 with their untagged equivalents (Fig. 1*B*). A specific interaction was observed between $MRS_{GST}$-His and AIMP3, and between $AIMP2_{GST}$-His and $EPRS_{GST}$. His-AIMP3 pulled down both $EPRS_{GST}$ and $MRS_{GST}$, whereas $EPRS_{GST}$-His interacted with both AIMP3 and $AIMP2_{GST}$. In contrast to previously known GST dimers, these GST domains appear to prefer heterodimer formation. Each of the mixtures of $MRS_{GST2}$-AIMP3, AIMP3-$EPRS_{GST2}$, and $EPRS_{GST2}$-$AIMP2_{GST2}$ was eluted from gel chromatography at the expected molecular size for a GST dimer (Fig. 1, *C–E*). The proteins in each peak were separated by gel electrophoresis at an equimolar ratio, further confirming the formation of 1:1 heterodimers. These results suggest that these GST domains form heterodimers rather than homodimers.

We investigated cellular interactions between the GST domains by FRET analysis using CFP and YFP (Fig. 3). We introduced the pairs of CFP-AIMP3:YFP-MRS, CFP-AIMP3:

**TABLE 1**
**Data collection and refinement statistics**

| | $MRS_{GST}$-AIMP3 | AIMP3-$EPRS_{GST}$ | $EPRS_{GST}$-$AIMP2_{GST}$ |
|---|---|---|---|
| **Data collection** | | | |
| X-ray source | PAL 7A | PAL 5C | PAL 5C |
| Wavelength (Å) | 0.9793 | 0.9796 | 0.9796 |
| Space group | P222 | P3 | $P2_12_12_1$ |
| Unit-cell parameters (Å) | 43.22 71.43 116.16 | 92.06 92.06 185.95 | 94.67 111.77 181.25 |
| Resolution (Å) | 50.0 – 1.6 (1.60 – 1.66)[a] | 50.0 – 2.6 (2.60 – 2.69)[a] | 50.0 – 2.6 (2.60 – 2.69)[a] |
| Total reflections | 419,334 | 291,301 | 395,565 |
| Unique reflections | 43,517 | 53,953 | 59,779 |
| Redundancy | 9.6 (8.9) | 5.4 (5.0) | 6.6 (5.9) |
| Completeness (%) | 89.2 (94.4) | 100 (100) | 99.7 (99.9) |
| $R_{sym}$ | 0.101 (0.535) | 0.157 (0.852) | 0.154 (0.886) |
| Average $I/\sigma$ ($I$) | 24.4 (3.6) | 16.5 (2.8) | 17.4 (2.6) |
| **Refinement details** | | | |
| Space group | $P22_12_1$ | $P3_1$ | $P2_12_12_1$ |
| Resolution (Å) | 30.49 − 1.60 | 48.93 – 2.60 | 42.50 – 2.60 |
| Reflection (working) | 41,292 | 51,915 | 59,630 |
| Reflection (test) | 2,189 | 1,980 | 1,998 |
| $R_{work}$ (%) | 21.8 | 13.8 | 18.9 |
| $R_{free}$ (%) | 24.7 | 17.0 | 24.7 |
| No. of water molecules | 178 | 6 | 67 |
| No. of I3C | 3 | | |
| No. of GOL | | | 2 |
| Root mean square deviation from ideal geometry | | | |
| Bond length (Å) | 0.008 | 0.011 | 0.009 |
| Bond angle (°) | 1.308 | 1.538 | 1.201 |
| Average $B$ factors (Å) | | | |
| Molecule A (main/side chain) | 20.73 (19.73/21.74) | 22.70 (22.66/22.75) | 72.32 (70.38/74.45) |
| Molecule B (main/side chain) | 16.43 (15.70/17.15) | 37.09 (37.67/36.46) | 76.04 (76.42/75.62) |
| Molecule C (main/side chain) | | 22.19 (22.10/22.28) | 63.15 (60.89/65.57) |
| Molecule D (main/side chain) | | 39.03 (39.54/38.50) | 79.54 (76.37/79.74) |
| Molecule E (main/side chain) | | 22.86 (22.73/22.99) | 60.71 (57.88/63.72) |
| Molecule F (main/side chain) | | 44.71 (45.68/43.66) | 65.00 (64.39/65.67) |
| Molecule G (main/side chain) | | 24.06 (24.22/23.90) | 74.64 (73.06/76.37) |
| Molecule H (main/side chain) | | 45.90 (47.73/43.89) | 91.40 (93.11/89.42) |
| Water | 21.60 | 38.90 | 58.94 |
| I3C | 23.61 | | |
| Glycerol | | | 107.90 |

[a] Values in parentheses are for highest-resolution shell.

YFP-EPRS, CFP-AIMP2:YFP-EPRS, and CFP-HRS (histidyl-tRNA synthetase):YFP-MRS as negative control into CHO-K1 cells and monitored the FRET signal. The pairs of AIMP3:MRS, AIMP3:EPRS, and AIMP2:EPRS showed high FRET efficiencies with averages of 80.2 ($n = 37$), 75.8 ($n = 34$), and 80.8% ($n = 40$), respectively, whereas the non-interaction pair of HRS:MRS showed a FRET efficiency of only 0.9% ($n = 27$), further suggesting the formation of AIMP3-MRS, AIMP3-EPRS, and EIMP2-EPRS complexes.

*Crystal Structures of the GST Domains*—To understand the molecular details for the GST-mediated complex formation, we determined the heterodimeric complex structures of $MRS_{GST}$-AIMP3, AIMP3-$EPRS_{GST}$, and $EPRS_{GST}$-$AIMP2_{GST}$ at a resolutions of 1.6, 2.6, and 2.6 Å, respectively (Table 1), and analyzed the monomeric structures first. Although all four GST domains adopt a GST-fold consisting of the N and C subdomains (Fig. 4, *A–D*), MRS and EPRS contain a canonical four-stranded β-sheet, corresponding to that of the canonical thioredoxin-fold, in their GST-N subdomains, whereas AIMP3 and AIMP2 have a three- and five-stranded β-sheet, respectively. Unlike human GSTθ, which has an α-helix that completes the α-β-α thioredoxin structure inserted between the β2 and β3 strands (27), MRS, EPRS, AIMP2, and AIMP3 lack the helix in the β-sheet, although MRS retains the long β2-β3 loop (Fig. 4, *E–I*).

The AIMP3 structures in the complexes with $MRS_{GST}$ and $EPRS_{GST}$ are essentially identical to the previously determined structure of AIMP3 alone (28), suggesting little conformational change from the complex formation. AIMP3 adopts an α-helical bundle structure with the central α5 helix surrounded by helices from GST-C and GST-N (Fig. 4*A*). Its α7 helix is perpendicular to the other helices and is followed by a long C-terminal tail. Compared with AIMP3, $MRS_{GST}$ contains a helix bundle with a long kinked α3 helix (α3A and α3B), and lacks the short α6 helix of AIMP3 situated between the central α5 and the next helix (Fig. 4*B*). MRS has two additional helices (α7 and α8) at its C terminus, whereas AIMP3 has a flexible C-terminal peptide. The last helix α8 is situated between GST-N and GST-C, as observed in human GSTθ. The structure of $EPRS_{GST}$ in the complex of AIMP3-$EPRS_{GST2}$ is almost identical to that in the $EPRS_{GST2}$-$AIMP2_{GST1}$ complex. $EPRS_{GST}$ has a relatively short β2-β3 loop compared with $MRS_{GST}$. GST-C of $EPRS_{GST}$ has a helix (α6) linking central α5 and perpendicular α7 helices and its C-terminal tail forms α8 helix (Fig. 4*C*). AIMP2 has a larger GST-N than others. Its GST-N is comprised of a five-stranded β-sheet and three helices with an additional helix-loop-strand motif inserted between the first helix and the following strand (Fig. 4*I*). It has a relatively short β3-β4 loop and no helix connecting the central (α6) and perpendicular helix (α7) in GST-C (Fig. 4*D*).

*GST Heterodimerization via Interface 1*—The structures of the $MRS_{GST}$-AIMP3 and $EPRS_{GST}$-$AIMP2_{GST}$ complexes reveal that the GST heterodimerization is formed by a helical bundle involving the α2 and α3 helices (α3 and α4 helices for

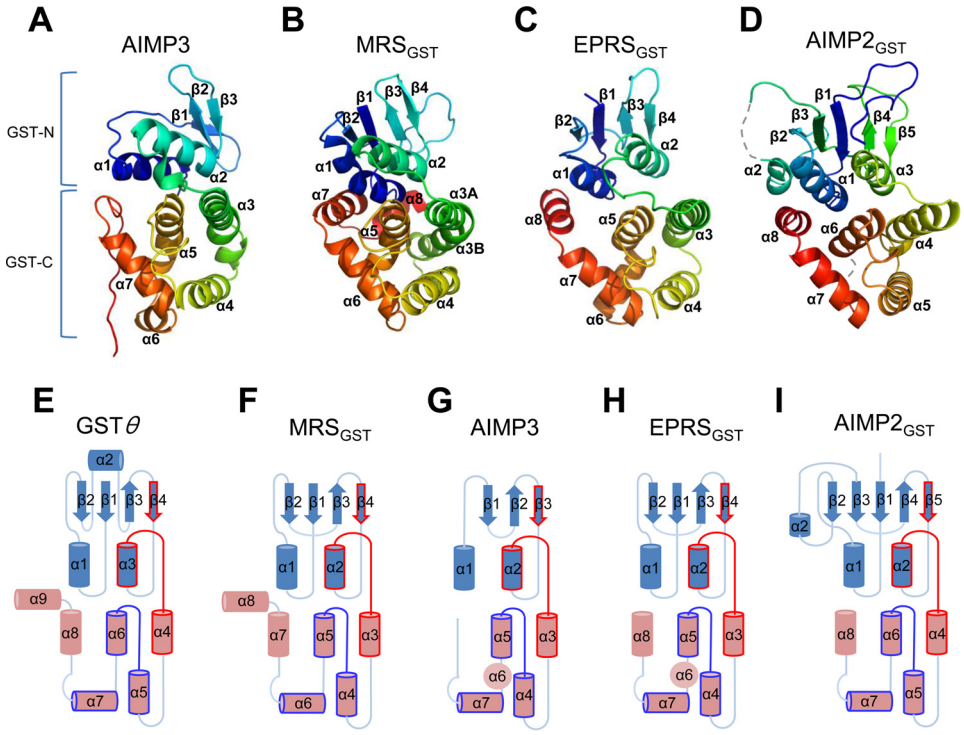


FIGURE 4. **Structures of the monomeric GST domains.** *A-D*, ribbon diagrams of the GST domains of AIMP3 (*A*), MRS (*B*), EPRS (*C*), and AIMP2 (*D*). All four GST domains consist of GST-N and GST-C subdomains. The rainbow color (*blue* to *red*) represents the N terminus to the C terminus of the proteins. *E-I*, topology diagrams of the GST domains of human GST$\theta$ (*E*), MRS (*F*), AIMP3 (*G*), EPRS (*H*), and AIMP2 (*I*). AIMP3 contains a three-stranded $\beta$-sheet missing a strand at the N terminus of the first $\alpha$-helix. MRS$_{GST}$ and EPRS$_{GST}$ have a canonical four-stranded $\beta$-sheet and AIMP2$_{GST}$ has a five-stranded $\beta$-sheet formed by insertion of a strand-loop-helix motif between the first $\alpha$-helix and the following $\beta$-strand of the canonical GST-N. The $\beta$-hairpin structure and the second $\alpha$-helix for binding interface 1 (*red lines*) are structurally conserved. In contrast to GST$\theta$, which contains a long structural motif with a helix between $\beta$2 and $\beta$3 strands, the four GST domains have a relatively short loop and no helix. The binding interface 2 is indicated by *blue lines*.

AIMP2) (Fig. 5, *A* and *B*). Two GST domains in the complexes are related by 2-fold rotational pseudo-symmetry. It is similar to the canonical GST homodimer.

In the MRS$_{GST}$-AIMP3 complex, $\alpha$3A of MRS and $\alpha$3 helices from AIMP3 come into close contact with one another through the interaction of small residues such as Ala-64 of MRS and Ala-69 of AIMP3 (Fig. 5*D*). There is an additional interaction between GST-N of MRS ($\beta$-sheet) and GST-C of AIMP3 ($\alpha$4 helix) (Fig. 5*A*). MRS $\beta$4 strand is inserted between $\alpha$3 and $\alpha$4 helices of AIMP3, and the side chain of Gln-73 from the $\alpha$3 helix has hydrogen bonds with the main chain of the $\beta$4 strand. The long $\beta$2-$\beta$3 loop of MRS contacts the $\alpha$4 helix of AIMP3 (Figs. 5*A* and 6*A*), whereas limited interaction is seen between GST-N of AIMP3 and GST-C of MRS. The surface potential of the binding interfaces from the heterodimer shows that the binding is mainly mediated through polar interactions between helices $\alpha$2 and $\alpha$3, and hydrophobic contacts between GST-N of MRS and GST-C of AIMP3 (Fig. 6*B*). For example, charged residues, Arg-67, Asp-79, Glu-86 and Glu-91 of MRS and Arg-28, Lys-53, Glu-76, and Asp-97 of AIMP3 participate in the interaction (Fig. 5*D*). At the center of the 2-fold pseudo-symmetry a stacking of side chains was found between MRS Arg-67 and AIMP3 Gln-72 from both $\alpha$3 helices. The A64R and E86R mutations of MRS$_{GST2}$ and the Q73R mutation of AIMP3 ablated the interaction between the two proteins, validating the binding interface of MRS and AIMP3, as observed in the crystal structure (Fig. 5*G*).

In the EPRS$_{GST}$-AIMP2$_{GST}$ complex, an additional contact is made between the N subdomain ($\beta$-sheet of AIMP2$_{GST1}$) and the C subdomain ($\alpha$4 helix of EPRS$_{GST2}$), similar to that observed in the MRS$_{GST}$-AIMP3 complex (Fig. 5*B*). The long $\beta$4-$\beta$5 loop and $\beta$5 strand of AIMP2$_{GST1}$ are inserted between the $\alpha$3 and $\alpha$4 helices of EPRS$_{GST2}$, and the loop connecting strands $\beta$3 and $\beta$4 extends to the $\alpha$4 helix of EPRS$_{GST2}$ (Fig. 6*C*). The $\beta$4 to $\beta$5 motif of AIMP2$_{GST1}$ and an additional peptide region of AIMP2 at the N terminus of the $\beta$1 strand make hydrophobic contacts with the N terminus of EPRS$_{GST2}$ $\alpha$3 helix. Surface potentials of the interaction interface between the two proteins show charged interactions of AIMP2$_{GST1}$ $\alpha$3 and $\alpha$4 helices with the EPRS$_{GST2}$ $\alpha$2 and $\alpha$3 helices (Fig. 6*D*). These involve residues Arg-56, Arg-60, and Asp-79 from EPRS, and Arg-215, Asp-234, and Asp-238 from AIMP3 (Figs. 5*E* and 6*D*). As observed in the MRS$_{GST}$-AIMP3 complex, a stacking interaction of the side chains from two arginine residues, Arg-56 in EPRS$_{GST2}$ $\alpha$2 helix and Arg-215 in AIMP2$_{GST1}$ $\alpha$3 helix occurred at the center of pseudo 2-fold symmetrical axis in the heterodimer. The binding interfaces were further validated by an *in vitro* pulldown assay. Among the mutants tested, the R215A and D238R mutations of AIMP2$_{GST1}$ and R56A mutation of EPRS$_{GST2}$ abolished the interaction, whereas the mutations in other surfaces did not (Fig. 5*H*).

*GST Heterodimerization via Interface 2*—Four AIMP3-EPRS$_{GST}$ complexes were found in the crystal asymmetric unit.

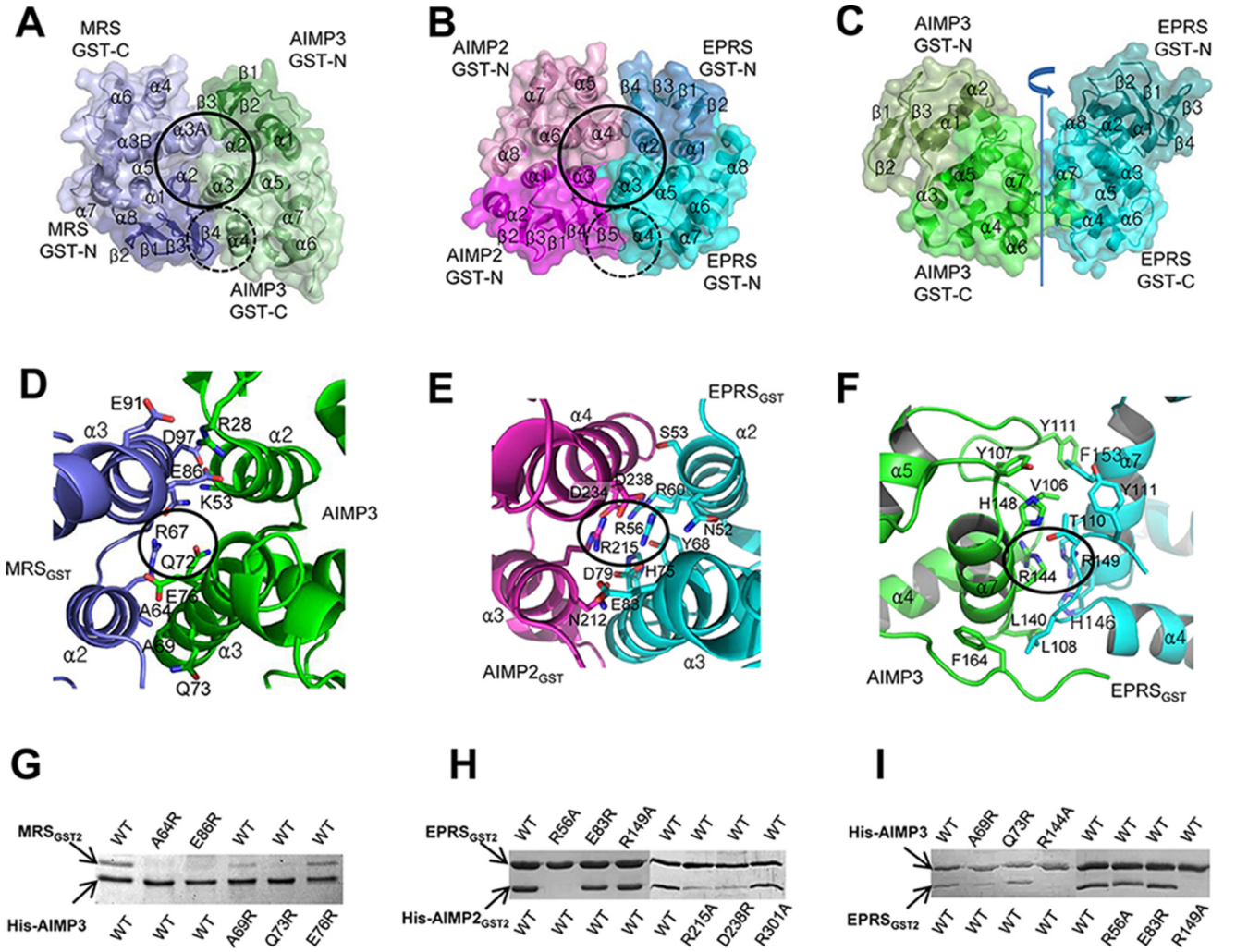


FIGURE 5. **Structures of the binary GST domain complexes I.** *A* and *B*, the heterodimers of MRS$_{GST}$-AIMP3 (*A*) and EPRS$_{GST2}$-AIMP2$_{GST2}$ (*B*). The dimer interface primarily involves a four-helix bundle-like structure formed by two helices from each protein (*solid circle*). Additional contacts occur between GST-N and GST-C subdomains (*dotted circle*). *C*, the AIMP3ΔC5-EPRS$_{GST2}$ heterodimer is formed through the GST-C subdomains and positions the two proteins in pseudo 2-fold symmetry. The α7 helices of both proteins are located at the binding interface, parallel to the symmetry axis. *D-F*, binding interfaces in the heterodimers. Charged and polar residues are involved in the binding between MRS$_{GST}$ and AIMP3 (*D*) and between EPRS$_{GST}$ and AIMP2$_{GST}$ (*E*), whereas the residues at the interface of the AIMP3-EPRS$_{GST}$ complex (*F*) are mainly involved in hydrophobic interactions. Stacking of two planar side chains is found at the center of pseudo 2-fold symmetric axis (circle). *G-I*, the mutational effects of GST domains on complex formation were determined by *in vitro* pulldown assay using His-AIMP3 for MRS$_{GST2}$ (*G*) and EPRS$_{GST2}$ (*H*), and using AIMP2$_{GST2}$-His for EPRS$_{GST2}$ (*I*).

All four interactions between AIMP3 and EPRS$_{GST}$ are established in an identical manner via their GST-C subdomains. The binding interfaces of both AIMP3 and EPRS$_{GST}$ consist of α7 helices and the loop connecting α4 and α5 helices, and the two proteins are oriented in pseudo 2-fold symmetry (Figs. 5*C* and 6*E*). This is similar to the interaction between two AIMP3s, which form an asymmetric unit via their binding interface 2 found in the AIMP3 crystal structure (28). Surface potential analysis indicates low electric potentials at the binding area, suggesting that the interaction between two proteins takes place mainly through hydrophobic contacts (Fig. 6*F*). A few hydrogen bonds between polar residues help the positioning of some side chains, including Tyr-107, Tyr-111, Phe-164, Val-106, and Leu-140 of AIMP3, and Tyr-111, Phe-153, His-146, and Leu-108 of EPRS (Fig. 5*F*). There is stacking of arginine side chains from α7 helices, Arg-144 of AIMP3 and Arg-149 of EPRS, at the axis of the pseudo 2-fold symmetry (Fig. 6*E*). We introduced mutations at interfaces 1 and 2 of AIMP3 and EPRS, and tested their effect on the interaction. Among these mutants, only R144A of AIMP3 and R149A of EPRS ablated complex formation between the two proteins (Fig. 5*I*).

*Multimeric Complexes of GST Domains*—Because AIMP3 can use different binding interfaces to form heterodimers with MRS$_{GST}$ and EPRS$_{GST}$, we examined whether AIMP3 could form a heterotrimer with both proteins. His-AIMP3 was mixed with MRS$_{GST2}$ and EPRS$_{GST2}$, and the mixture was passed through a Ni-NTA column. SDS-PAGE analysis of the His-AIMP3 eluted fraction showed the three proteins were present with comparable band densities, indicating that AIMP3 can bind to both MRS$_{GST2}$ and EPRS$_{GST1}$ simultaneously (Fig. 7*A*). Similarly, we checked whether EPRS$_{GST}$ could bind to both AIMP2$_{GST}$ and AIMP3 simultaneously. All three proteins were present in the eluent from the Ni-NTA column at an approximately equal ratio (Fig. 7*B*). To further elucidate the complexes, we subjected the mixture of the three purified proteins

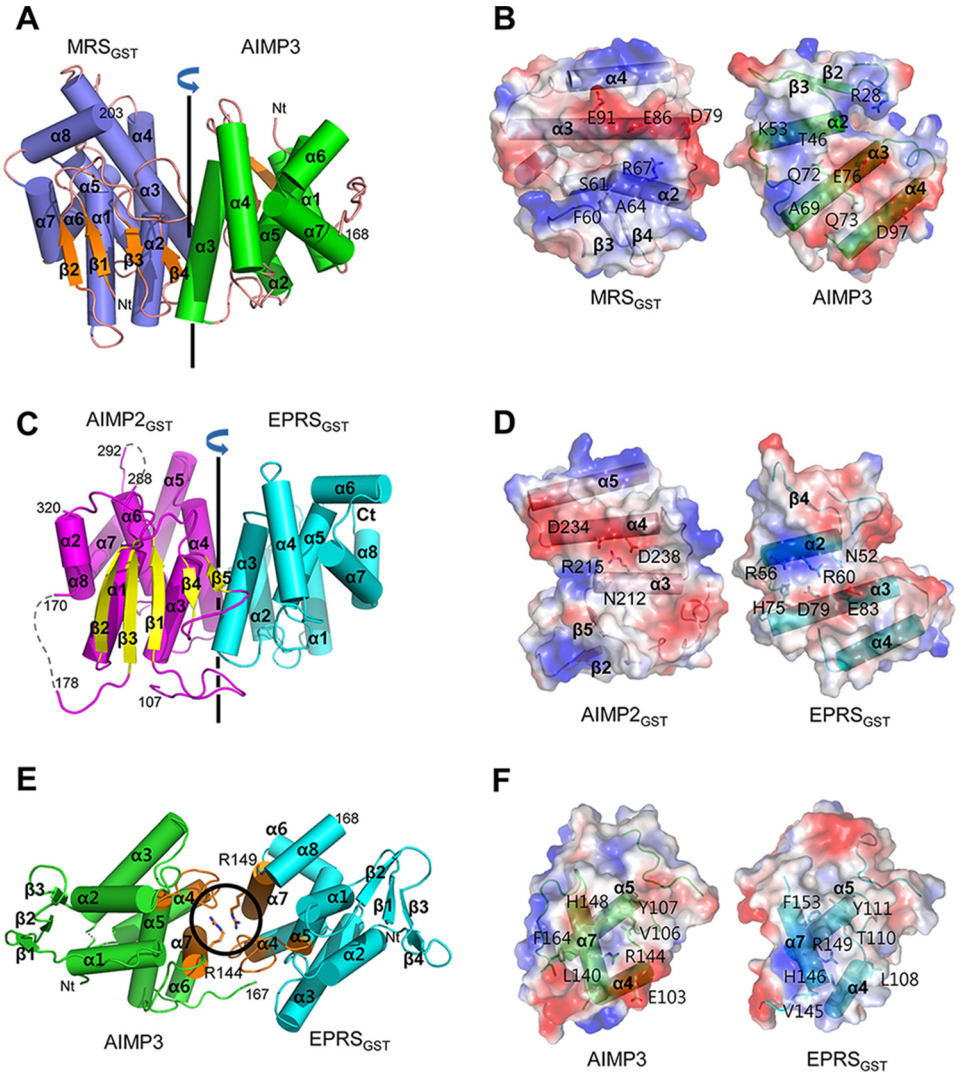


FIGURE 6. **Structures of the binary GST domain complexes II.** *A*, helix arrangement in the MRS$_{GST}$-AIMP3 complex. The binary complex displays pseudo 2-fold symmetry with the $\alpha$2 and $\alpha$3 helices from each protein positioned in parallel to the symmetry axis. Only the N-terminal portion of the $\alpha$3-helices is involved in the complex interaction. *B*, negative (*blue*) and positive (*red*) surface potentials of the binding interfaces in the MRS$_{GST}$-AIMP3 complex indicate the charged interactions of the area. *C*, helix arrangement in the EPRS$_{GST}$-AIMP2$_{GST}$ complex. The two proteins are in pseudo 2-fold symmetry with the symmetry axis parallel to the helices in the interface. The peptide N-terminal to the $\beta$1 strand and the long $\beta$4-$\beta$5 loop of AIMP2$_{GST}$ wrap the N terminus of the $\alpha$3 helix of EPRS$_{GST}$. *D*, surface potentials of the binding interfaces in the EPRS$_{GST}$-AIMP2$_{GST}$ complex. Negative (*blue*) and positive (*red*) potentials and residues critical for the interaction are indicated. *Arrows* show the split direction of the dimer. *E*, helix arrangement in the AIMP3-EPRS$_{GST}$ complex. The loop connecting $\alpha$4 and $\alpha$5 helices, and $\alpha$7 helix form the binding interface (*brown*). Arginine side chains from the $\alpha$7 helices are stacked at the center of the binding interface (circle). *F*, surface potentials of binding interfaces in the AIMP3-EPRS$_{GST}$ complex showing non-polar contact areas. *Arrows* show the split direction of the dimer. Negative (*blue*) and positive (*red*) potentials are indicated.

(MRS$_{GST2}$-His, EPRS$_{GST3}$-His, and His-AIMP3) to gel filtration chromatography. The three proteins eluted as a single peak at 112 kDa, a size compatible with that of the 2:2:2 heterotrimeric complex (Fig. 7*D*) and the peak fraction contained all three proteins at a similar molar ratio in gel electrophoresis. The mixture of EPRS$_{GST3}$-His, AIMP2$_{GST2}$-His, and His-AIMP3 also eluted as a single peak from gel filtration chromatography at 61 kDa, a size compatible with that of a 1:1:1 heterotrimeric complex (Fig. 7*E*).

Because the two heterotrimers have AIMP3 and EPRS in common, there is a possibility that the four GST proteins form a heterotetrameric complex. We tested this possibility by repeating the pulldown methods described above with a mixture of His-AIMP3, MRS$_{GST2}$, EPRS$_{GST2}$, and AIMP2$_{GST2}$. All four proteins were co-purified as a complex, as shown by SDS-PAGE (Fig. 7*C*). In the gel filtration chromatography using a mixture of MRS$_{GST2}$-His, AIMP2$_{GST2}$-His, EPRS$_{GST3}$-His, and His-AIMP3, the proteins eluted as a single peak at a volume corresponding to the size of a 1:1:1:1 hetero-tetramer (Fig. 7*F*).

To generate a model for the tetrameric complex of MRS$_{GST}$-AIMP3-EPRS$_{GST}$-AIMP2$_{GST}$, two heteroternary complexes, MRS$_{GST}$-AIMP3-EPRS$_{GST}$ and AIMP3-EPRS$_{GST}$-AIMP2$_{GST}$, were initially modeled by superimposition of AIMP3 and EPRS$_{GST}$, respectively. No contact between MRS$_{GST}$ and EPRS$_{GST}$ was observed in the model of MRS$_{GST}$-AIMP3-EPRS$_{GST}$, whereas AIMP3 and AIMP2$_{GST}$ were predicted to have extra contacts between each other in the model of AIMP3-EPRS$_{GST}$-AIMP2$_{GST}$ (Fig. 8, *A* and *B*). The C-terminal tail of AIMP3 meets the $\beta$4-$\beta$5 loop of AIMP2$_{GST}$ in the vicinity of the

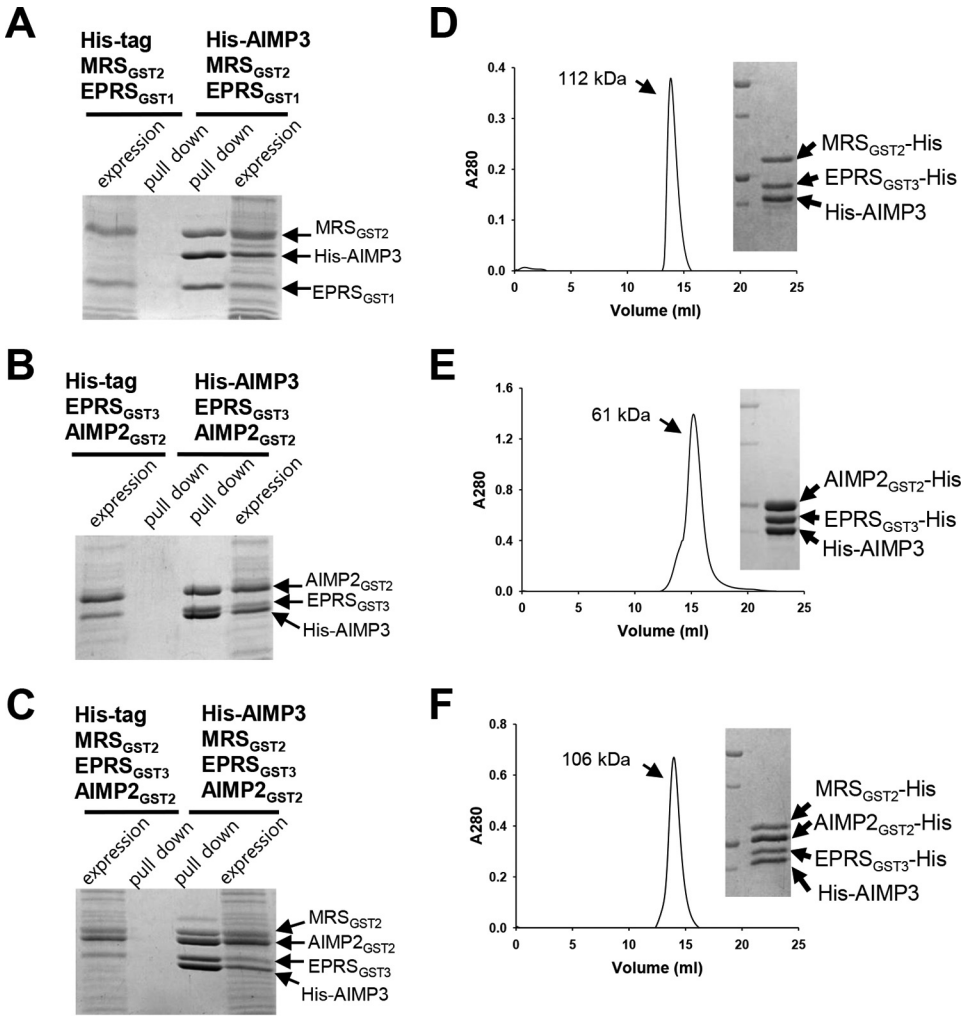


FIGURE 7. **Multiple complexes of GST domains.** *A*, His-AIMP3, MRS$_{GST2}$, and EPRS$_{GST1}$ were mixed and purified on an Ni-NTA column and the co-purification of these proteins was monitored by SDS-PAGE. The His tag alone was used as a negative control to ensure that the presence of the three proteins was the result of complex formation. *B*, His-AIMP3 was mixed with AIMP2$_{GST2}$ and EPRS$_{GST3}$ and co-purification of the three proteins was carried out and confirmed as above. *C*, His-AIMP3 was purified with MRS$_{GST2}$, EPRS$_{GST3}$, and AIMP2$_{GST2}$, and characterized as above. *D-F*, size exclusion chromatography of the mixtures of three proteins, MRS$_{GST2}$-His, EPRS$_{GST3}$-His, and His-AIMP3 (*D*), or His-AIMP3, His-EPRS$_{GST3}$ and AIMP2$_{GST2}$-His (*E*), and four proteins, MRS$_{GST2}$-His, AIMP2$_{GST2}$-His, EPRS$_{GST3}$-His, and His-AIMP3 (*F*) by a Superdex G200 column. All the proteins were eluted together at the marked size and the peak contained all the proteins at the same molar ratio (*right*).

C terminus of the $\alpha$4 helices of EPRS$_{GST}$. The N-terminal peptide region located before the $\beta$1 strand of AIMP2$_{GST}$ extends to the $\alpha$7 helix and following the tail of AIMP3 over the $\alpha$3 helix of EPRS. This region could provide further specificity for the formation of this ternary complex. For the tetrameric complex, three heterodimeric complex structures were placed by simultaneous superimpositions of AIMP3 and EPRS (Fig. 8*C*). This produced a linear MPS$_{GST}$-AIMP3-EPRS$_{GST}$-AIMP2$_{GST}$ complex without clashes between MRS$_{GST}$ and AIMP2$_{GST}$. Thus, the tetrameric GST complex was formed by alternative usage of the binding interfaces of GST domains. The linear arrangements of four GST domains through their binding interface 1 and 2 were observed in the asymmetric units of the AIMP3-EPRS$_{GST}$ and EPRS$_{GST2}$-AIMP2$_{GST1}$ complex crystals.

*The Tetrameric GST Domain Complex as a Scaffold*—Multimeric assembly of GST domains would be affected in the full-length proteins depending on the orientation of the other peptides attached to them. The catalytic domains of MRS and EPRS are several times bigger in size than GST domains. However, in the heterotetrameric complex of MRS$_{GST}$-AIMP3-EPRS$_{GST}$-AIMP2$_{GST}$, the N- and C-terminal ends of the GST domains are oriented so that the attached catalytic and functional domains can be positioned without steric hindrance (Fig. 8*D*). To determine whether this tetrameric GST complex could serve as a scaffold, full-length MRS and EPRS$_{GST4}$ containing the ERS catalytic domain were used to form a tetrameric complex with AIMP3 and AIMP2$_{GST2}$. The mixture of full-length MRS, His-EPRS$_{GST4}$, His-AIMP3, and His-AIMP2$_{GST2}$ was eluted from a gel filtration column as a single peak at a molecular size of around 290 kDa, the size predicted for a 1:1:1:1 tetrameric complex of the four proteins (Fig. 8*E*), suggesting that the GST tetramer can be formed with full-length proteins.

To observe the three-dimensional morphology of these complexes, we subjected the MRS$_{GST2}$-AIMP3-EPRS$_{GST2}$-AIMP2$_{GST1}$ and MRS-AIMP3-EPRS$_{GST4}$-AIMP2$_{GST2}$ tetramers to electron microscopic analysis followed by three-dimen-

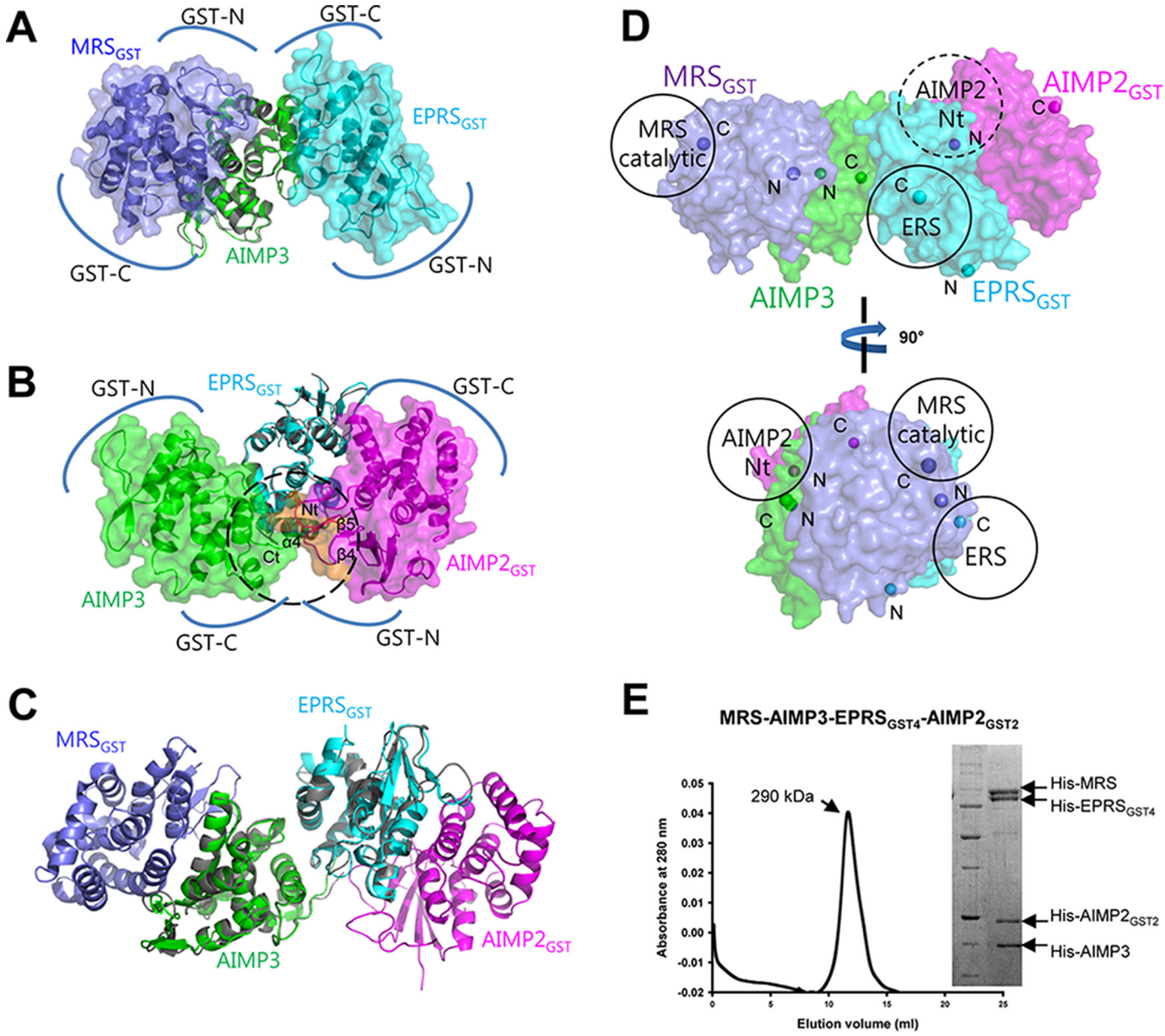


FIGURE 8. **Tetrameric GST domain complex as a scaffold.** *A*, structures of the MRS$_{GST1}$-AIMP3 (*slate-green*) and AIMP3-EPRS$_{GST2}$ (*gray-cyan*) complexes are superimposed based on the structure of AIMP3. The wedge-shaped arrangement of AIMP3 enables the proximal localization of the MRS GST-N and EPRS GST-C subdomains. *B*, structures of AIMP3-EPRS$_{GST2}$ (*green-gray*) and EPRS$_{GST2}$-AIMP2$_{GST2}$ (*cyan-magenta*) complexes are superimposed based on the structure of EPRS$_{GST2}$. Similar to the MRS$_{GST1}$-AIMP3-EPRS$_{GST2}$ complex, AIMP3 GST-C and AIMP2 GST-N subdomains are located close to one another (*dotted circle*). The N-terminal peptide and $\beta$4-$\beta$5 loop of AIMP2 (colored in *orange* and *magenta*, respectively) contact the C terminus of AIMP3. *C*, the structures of MRS$_{GST}$-AIMP3, AIMP3-EPRS$_{GST}$, and EPRS$_{GST}$-AIMP2$_{GST}$ complexes were superimposed to generate the tetrameric complex connecting MRS-AIMP3-EPRS-AIMP2. AIMP3-EPRS$_{GST}$ (*gray-gray*) matches to AIMP3 and EPRS$_{GST}$ from MRS$_{GST}$-AIMP3 (*slate-green*) and EPRS$_{GST}$-AIMP2$_{GST}$ (*cyan-magenta*) complexes, respectively. *D*, spatial orientation of the remaining domains (MRS catalytic, ERS catalytic, and the N-terminal peptide of AIMP2) attached to the tetrameric GST complex of the MSC components. The N-terminal peptide of AIMP2 (*dotted circle*) is facing the side opposite to the catalytic domains of MRS and ERS (*circle*). *E*, the mixture of His-tagged full-length MRS, His-EPRS$_{GST4}$, His-AIMP2$_{GST2}$, and His-AIMP3 were subjected to Superdex G200 gel filtration chromatography. The four proteins were eluted together at a size of about 290 kDa, corresponding to the approximate size of an equimolar heterotetrameric complex. The proteins in the peak were separated by SDS-PAGE.

sional single particle analysis. Using selected individual particles of the tetrameric complexes from negatively stained fields, two-dimensional class averages and three-dimensional reconstructions of both complexes were generated (Fig. 9). When surface views of the reconstructed three-dimensional density map were compared with the two-dimensional class averages and raw particle images, three-dimensional density maps from both tetrameric complexes were consistent with the raw data, rendering the generated three-dimensional density maps reliable for further analysis (Fig. 9, *C* and *D*). Based on the two-dimensional class averages and reconstructed three-dimensional electron density models, the GST tetramers appeared to be rod shaped with a size of about 100 × 50 Å$^2$, which is compatible with the modeled GST tetramer structure (Figs. 9*A* and 10*A*). The modeled tetramer based on the crystal structures of the heterodimer fits well in the density map generated by three-dimensional reconstruction (Fig. 10*C*). In the case of the MRS-AIMP3-EPRS$_{GST4}$-AIMP2$_{GST2}$ complex, the

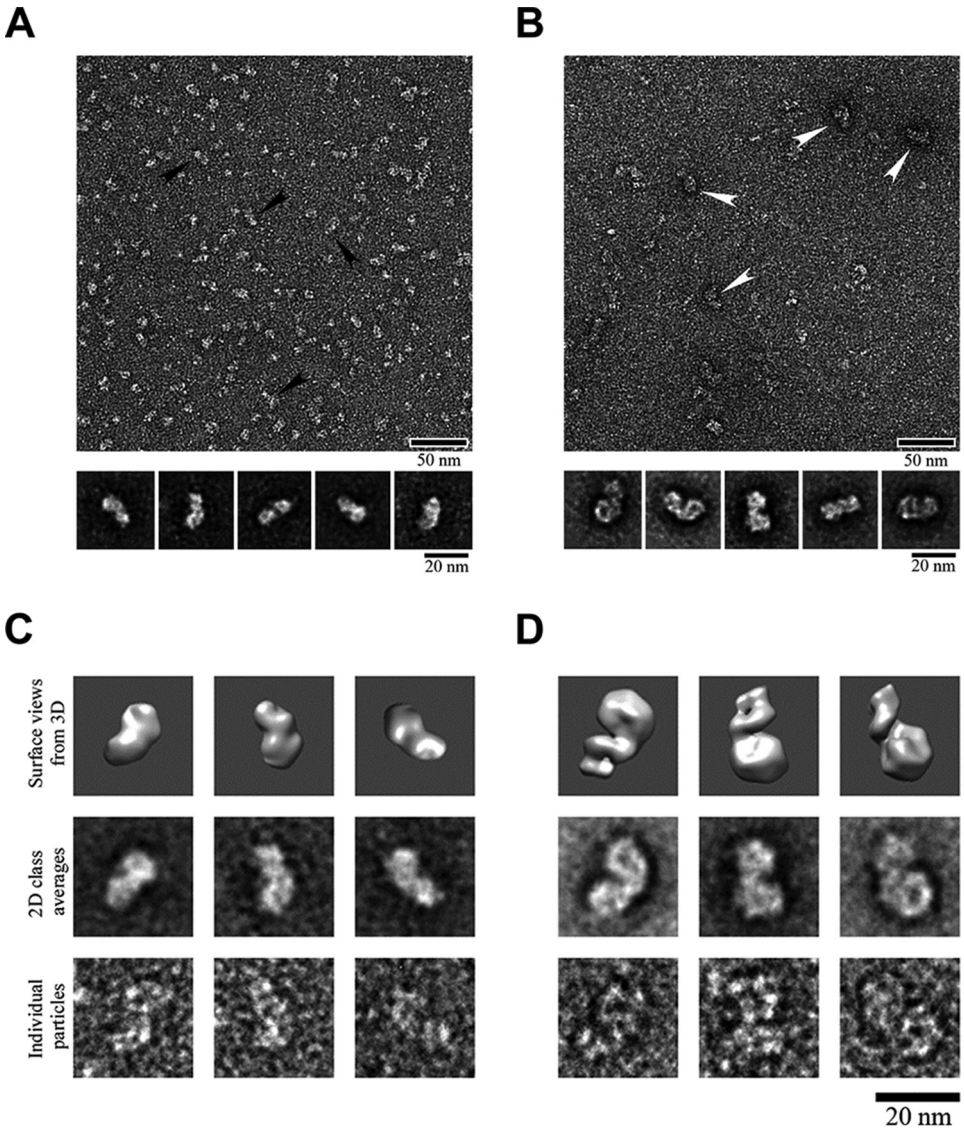


FIGURE 9. **Electron microscopy of the heterotetrameric complexes.** *A* and *B*, electron microscopy of tetrameric complexes. Negatively stained fields (*top*) of the $MRS_{GST2}$-AIMP3-$EPRS_{GST2}$-$AIMP2_{GST1}$ (*A*) and MRS-AIMP3-$EPRS_{GST4}$-$AIMP2_{GST2}$ (*B*) showing individual complex molecules (*arrowheads*) and representative two-dimensional averaged images (*bottom*) of the complex. The *scale bar* represents 50 (*top*) and 20 nm (*bottom*). *C* and *D*, comparison of raw particles (*bottom row*) with class averages (*middle row*) and the corresponding views of the three-dimensional reconstructed model (*top row*) of the $MRS_{GST2}$-AIMP3-$EPRS_{GST2}$-$AIMP2_{GST1}$ (*C*) and MRS-AIMP3-$EPRS_{GST4}$-$AIMP2_{GST2}$ (*D*) complexes. The *scale bar* represents 20 nm across all panels.

larger size of the observed particles suggests that the particle would encompass the catalytic domains of MRS and ERS (Figs. 9*B* and 10*B*). When the GST tetrameric complex was fitted into the three-dimensional reconstruction maps, sufficient densities remained on both sides to place the catalytic domains of MRS and ERS. The structure of the MRS-AIMP3-$EPRS_{GST4}$-$AIMP2_{GST2}$ complex was modeled by fitting homolog structures of MRS and ERS from *Pyrococcus abyssi* (29) and *Methanothermobacter thermoautotrophicus* (30), respectively, into the reconstructed three-dimensional map along with the structures of the GST tetramer (Fig. 10*D*).

*Dynamic Interaction between AIMP3 and $EPRS_{GST}$*—Although the sequential assembly of the GST domains of the four MSC components was demonstrated, dissociation of the MSC complex is a necessary step in the control of diverse cellular signaling pathways. For example, AIMP3 is a tumor suppressor that dissociates from MRS and translocates to the nucleus upon UV radiation (31). For AIMP3 to be released from the tetrameric complex, it also needs to dissociate from EPRS. The surface area at the binding interface of the AIMP3ΔC5-$EPRS_{GST2}$ complex is 760 $Å^2$, whereas that of the $MRS_{GST1}$-AIMP3ΔC5 and $ERPS_{GST2}$-$AIMP2_{GST1}$ complexes is ~1,200 $Å^2$ (Fig. 11). There are fewer residues involved in the interaction between AIMP3ΔC5 and $EPRS_{GST2}$ than in the $MRS_{GST1}$-AIMP3ΔC5 and $EPRS_{GST2}$-$AIMP2_{GST1}$ complexes. Thus, the affinity between AIMP3 and $EPRS_{GST}$, which occurs via binding interface 2, appears to be weaker than those between the subunits in $MRS_{GST}$-AIMP3 and $EPRS_{GST}$-$AIMP2_{GST}$ pairs, which employ binding interface 1.

Isothermal titration calorimetry (ITC) gave a $K_d$ value of 0.515 $\mu$M for equimolar binding between AIMP3 and $EPRS_{GST2}$ (Fig. 12*A*). There are possible interactions between AIMP3 and $AIMP2_{GST}$ in the model of the AIMP3-$EPRS_{GST}$-$AIMP2_{GST}$ ternary complex (see Fig. 8*B*). To evaluate whether the interac-

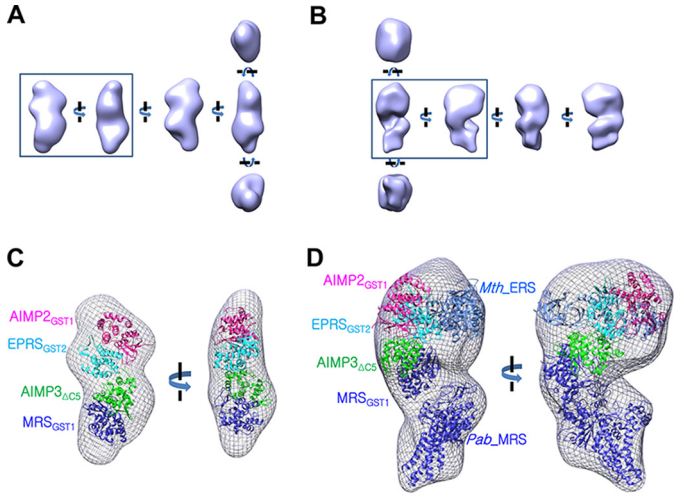


FIGURE 10. **Three-dimensional reconstruction of GST tetrameric complexes.** *A* and *B*, three-dimensional reconstructed models of the $MRS_{GST2}$-AIMP3-$EPRS_{GST2}$-$AIMP2_{GST1}$ (*A*) and the MRS-AIMP3-$EPRS_{GST4}$-$AIMP2_{GST2}$ (*B*) complexes. The models were rotated by 90 degrees around the *x* and *y* axes. *C*, structure of the tetrameric GST complex placed on the three-dimensional volumes reconstructed from electron microscopy. *D*, the MRS-AIMP3-$EPRS_{GST4}$-$AIMP2_{GST2}$ complex was modeled by fitting the three-dimensional reconstruction with the modeled structure of the GST tetramer and homologous structures of MRS and ERS from *P. abyssi* (*Pab*_MRS)(29) and *M. thermoautotrophicus* (*Mth*_MRS)(30), respectively.

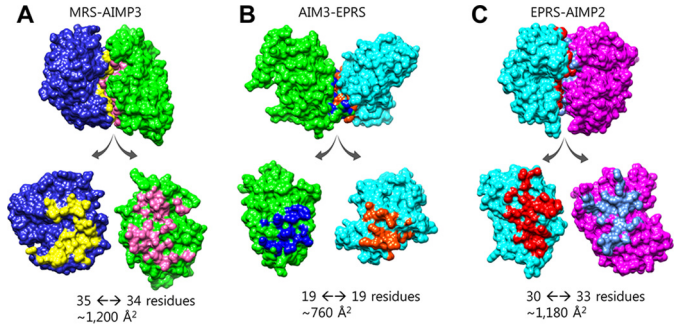


FIGURE 11. **The binding interfaces of heterodimeric complexes.** Contact areas in the three complexes, $MRS_{GST}$-AIMP3 (*A*), AIMP3-$EPRS_{GST}$ (*B*), and $EPRS_{GST}$-$AIMP2_{GST}$ (*C*), are highlighted with different colors to MRS (*blue*), AIMP3 (*green*), EPRS (*cyan*), and AIMP2 (*magenta*). The binding surface of the AIMP3-$EPRS_{GST}$ complex is smaller and the residues involved in the interaction are fewer than those observed in the $MRS_{GST}$-AIMP3 and $EPRS_{GST}$-$AIMP2_{GST}$ complexes.

tion between AIMP3 and $EPRS_{GST}$ is affected by the status of $EPRS_{GST}$, we measured the binding affinity between AIMP3 and $EPRS_{GST2}$ in the presence of $AIMP2_{GST2}$ and found that $EPRS_{GST2}$ remained practically unchanged ($K_d$ = 0.442 $\mu$M) (Fig. 12*B*). In the model of the $MRS_{GST}$-AIMP3-$EPRS_{GST}$ ternary complex, no additional interactions were expected to occur between $MRS_{GST}$ and $EPRS_{GST}$ (see Fig. 8*A*). However, the binding affinity of the AIMP3-$MRS_{GST2}$ complex for $EPRS_{GST2}$ increased ~3-fold ($K_d$ = 0.172 $\mu$M) (Fig. 12*C*). The AIMP3-$MRS_{GST2}$ complex also enhanced the binding affinity of AIMP3 for $EPRS_{GST2}$ complexed with $AIMP2_{GST2}$ ($K_d$ = 0.135 $\mu$M) (Fig. 12*D*). Although the conformation of AIMP3 was not significantly affected by its interaction with $MRS_{GST}$, B-factor (temperature factor) analysis suggests that the AIMP3 $\alpha$4-$\alpha$5 loop and $\alpha$7 helices, *i.e.* binding interface 2 for $EPRS_{GST}$, is stabilized when AIMP3 is complexed with $MRS_{GST}$ (Fig. 12*E*). However, binding of $AIMP2_{GST}$ does not seem to stabilize the binding interface 2 of $EPRS_{GST}$ for AIMP3 (Fig. 12*F*). These results indicate that MRS may positively affect complex formation between AIMP3 and EPRS. Conversely, dissociation of AIMP3 from EPRS could be facilitated in the absence of MRS.

## Discussion

We showed that the four different GST domains of MSC components can assemble together to form multisubunit complexes in an orderly fashion. Thus, this tetrameric complex can serve as a nucleation platform to which multiple proteins can be integrated. Eight different human ARSs form a MSC with three AIMPs. Although the structure of the whole complex is not yet solved, much progress has been made toward determining not only the structures of the individual components and subcomplexes, but also the overall shape of MSC and the stoichiometry of its components. Based on the tetrameric complex of the GST-containing proteins described in this work, the assembly of nine proteins, RRS, QRS, AIMP1, KRS, DRS, AIMP2, EPRS, AIMP3, and MRS in the MSC can be modeled (Fig. 13). The N-terminal peptide of AIMP2 complexed with the KRS homodimer (35) can be added to the N-terminal end of the AIMP2 GST domain via a polypeptide region containing an $\alpha$-helix. The ternary complex of QRS-AIMP1-RRS (32) can be attached to the KRS-AIMP2 complex via the leucine zipper between the N-terminal helices of AIMP1 and AIMP2 (33). Because PRS is covalently linked in EPRS and DRS tightly binds AIMP2 (36, 37), the presence of the two homodimers, PRS and DRS, suggests duplication of the MRS-AIMP3-ERPS-AIMP2 complex in an MSC. The ternary complex of QRS-AIMP1-RRS also has the potential to form a hexamer consisting of homodimers of each component (32). This subcomplex could be symmetrically duplicated and the stoichiometry of KRS:(AIMP2:AIMP1:DRS:ERPS:RRS):(MRS:AIMP3:QRS) would be 4:(2):(2). However, an MSC with a stoichiometry of 4:(2):(1) has also been suggested (38). Based on our own model, MRS and AIMP3 can be released from EPRS without significantly affecting the assembly of other MSC components because they are located at the periphery of the MSC. The dynamic affinity between AIMP3 and $EPRS_{GST}$ supports the release of the two components from the MSC. QRS is also weakly bound to MSC via its N-terminal helical interaction with the long helix of AIMP1 (32). Thus, linkage of the MSC subcomplex appears to accommodate both possible stoichiometries of the components. At this moment, it is not clear the exact location and stoichiometry of the remaining MSC components, leucyl-tRNA synthetase and isoleucyl-tRNA synthetase.

Considering that the protein synthesis machinery involves diverse cellular enzymes and regulatory factors, cells appear to have recruited GST domains as a tool for communication among translational components. In this work, we reveal the structure, dynamics, and mode of assembly of GST domains involved in protein-protein interactions. The novel heterotetrameric complex formed by GST domains in the MSC subcomplex provides an example of how GST domains can be used as a platform for the assembly of multicomponent protein complexes. The GST domains found in valyl-tRNA synthetase and cysteinyl-tRNA synthetase mediates its association with elongation factors (7, 39). As shown here, there is a potential for

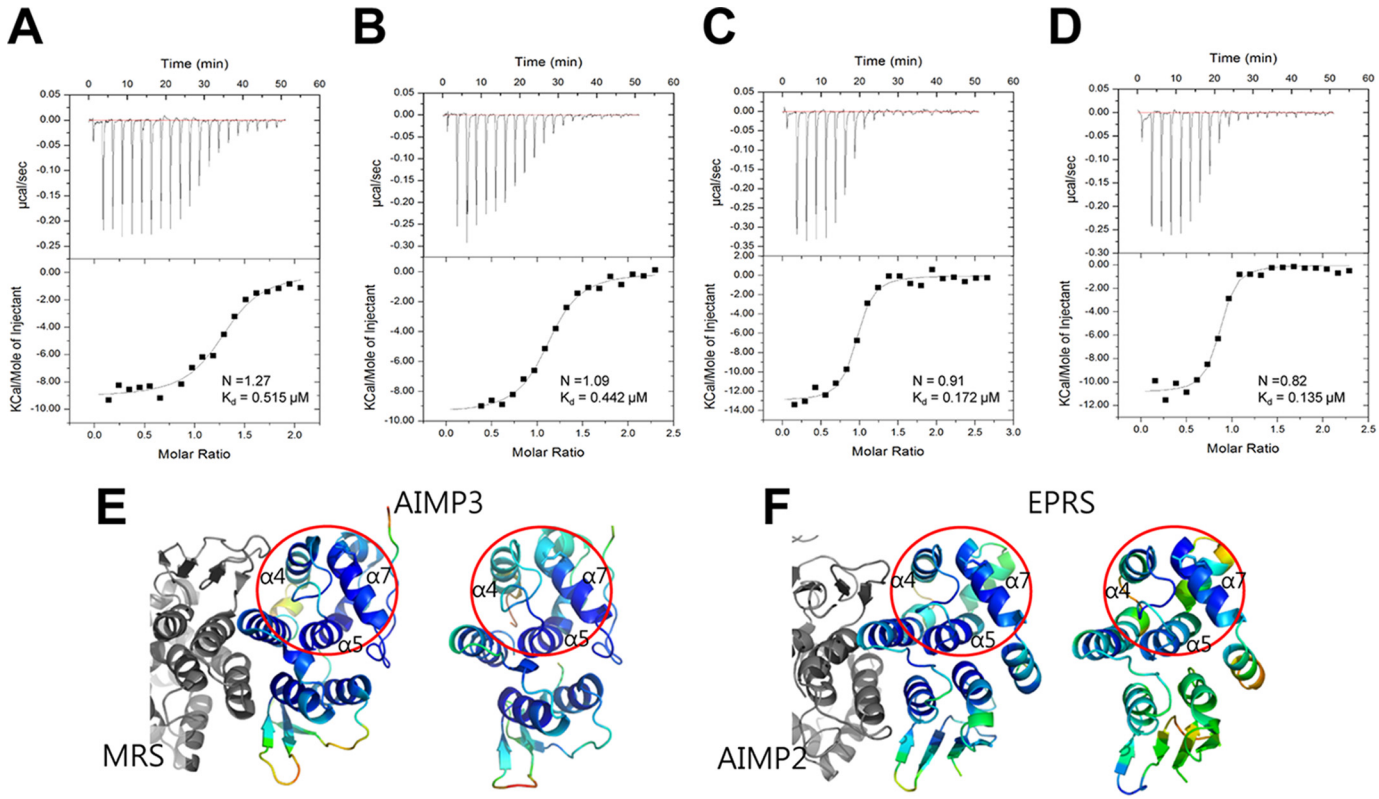


FIGURE 12. **Effects of MRS and AIMP2 on the interaction between AIMP3 and EPRS.** *A*, dissociation constant of the AIMP3 and $EPRS_{GST}$ complex, as measured by isothermal titration calorimetry. *B*, effect of $AIMP2_{GST}$ addition on the interaction between AIMP3 and $EPRS_{GST}$ as measured in *A*. *C*, effect of MRS addition on the interaction between AIMP3 and EPRS as determined in *A*. *D*, effect of $MRS_{GST}$ and $AIMP2_{GST}$ addition on the interaction of AIMP3 and $EPRS_{GST}$, as determined in *A*. *E*, the *B* factor values at the binding interface of AIMP3 (*red circle*) for $EPRS_{GST}$ (*right*) are decreased following interaction with $MRS_{GST}$ (*left*). *F*, the *B* factor values at the binding interface of $EPRS_{GST}$ (*red circle*) for AIMP3 (*left*) are not decreased by interaction with $AIMP2_{GST}$ (*right*). Low to high B factor values are colored *blue* to *red*.

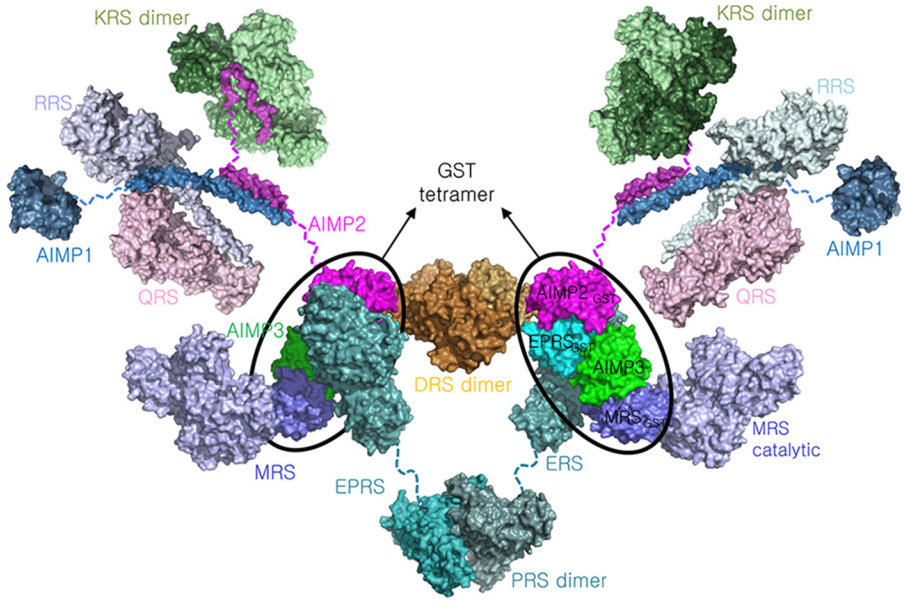


FIGURE 13. **Linkage of MSC components.** The heterotetrameric complex of the MRS-AIMP3-EPRS-AIMP2GST domains (marked with a *black circle*) is used as a platform for building the MSC model. The N-terminal peptide and a helix are linked to the GST domain of AIMP2 (*magenta*). The ternary complex of QRS-AIMP1-RRS (32) is attached to this platform via a leucine zipper located at the N-terminal region of AIMP1 and AIMP2 (33). The C-terminal domain of AIMP1 (34) (*blue*) is linked to the complex by a *dotted line*. The KRS dimer is hooked to the flexible N-terminal arm of AIMP2 (35). PRS linked to the C-terminal end of ERS can form a homodimer (36). The WHEP domains between ERS and PRS are replaced by a *short dotted line* (*cyan* and *dark cyan*). DRS (*orange*) is thought to be attached to AIMP2 that is located on the opposite face of KRS and can also form a homodimer (37). The MRS and ERS catalytic domains are modeled as shown in Fig. 10*D*. Assuming that most of the components have a potential to form dimers and KRS can form a tetramer (38), the whole arrangement of the components can be symmetrically duplicated. The two remaining components of MSC, leucyl- and isoleucyl-tRNA synthetases, are not included in this model.

complex formation via multiple GST domain assembly between the eEF1B complex and associated ARSs, and for communication between MSC and eEF1B mediated by the dynamic interactions of their GST domains.

*Author Contributions*—H. Y. C., S. J. M., H. J. C., Y. S. C., J. M. C., S. L., H. K. K., J. J. K., and C-Y. E. worked on collection and analysis of data, Y-G. K., M. G., and H. S. J. worked on conception and design; B. S. K. and S. K. provided conception and design, financial support, manuscript writing, and final approval of manuscript.

## References


1. Good, M. C., Zalatan, J. G., and Lim, W. A. (2011) Scaffold proteins: hubs for controlling the flow of cellular information. *Science* **322,** 680–686
2. Wilce, M. C., and Parker, M. W. (1994) Structure and function of glutathione *S*-transferases. *Biochim. Biophys. Acta* **1205,** 1–18
3. Oakley, A. J. (2005) Glutathione transferases: new functions. *Curr. Opin. Struct. Biol.* **15,** 716–723
4. Koonin, E. V., Mushegian, A. R., Tatusov, R. L., Altschul, S. F., Bryant, S. H., Bork, P., and Valencia, A. (1994) Eukaryotic translation elongation factor lγ contains a glutathione transferase domain: study of a diverse, ancient protein superfamily using motif search and structural modeling. *Protein Sci.* **3,** 2045–2054
5. Guo, M., and Yang, X. L. (2014) Architecture and metamorphosis. *Top. Curr. Chem.* **344,** 89–118
6. Simos, G., Segref, A., Fasiolo, F., Hellmuth, K., Shevchenko, A., Mann, M., and Hurt, E. C. (1996) The yeast protein Arc1p binds to tRNA and functions as a cofactor for the methionyl- and glutamyl-tRNA synthetases. *EMBO J.* **15,** 5437–5448
7. Kim, J. E., Kim, K. H., Lee, S. W., Seol, W., Shiba, K., and Kim, S. (2000) An elongation factor-associating domain is inserted into human cysteinyl-tRNA synthetase by alternative splicing. *Nucleic Acids Res.* **28,** 2866–2872
8. Robinson, J. C., Kerjan, P., and Mirande, M. (2000) Macromolecular assemblage of aminoacyl-tRNA synthetases: quantitative analysis of protein-protein interactions and mechanism of complex assembly. *J. Mol. Biol.* **304,** 983–994
9. Kim, J. H., Han, J. M., and Kim, S. (2014) Protein-protein interactions and multi-component complexes of aminoacyl-tRNA synthetases. *Top. Curr. Chem.* **344,** 119–144
10. Guo, M., Schimmel, P., and Yang, X. (2010) Functional expansion of human tRNA synthetases achieved by structural inventions. *FEBS Lett.* **584,** 434–442
11. Beck, T., Krasauskas, A., Gruene, T., and Sheldrick, G. M. (2008) A magic triangle for experimental phasing of macromolecules. *Acta Crystallogr. D* **64,** 1179–1182
12. Otwinowski, Z., and Minor, W. (1997) Processing of x-ray diffraction data collected in oscillation mode. *Methods Enzymol.* **276,** 307–326
13. Terwilliger, T. C., and Berendzen, J. (1999) Automated MAD and MIR structure solution. *Acta Crystallogr. D* **55,** 849–861
14. Terwilliger, T. C. (2000) Maximum-likelihood density modification. *Acta Crystallogr. D* **56,** 965–972
15. Emsley, P., and Cowtan, K. (2004) Coot: model-building tools for molecular graphics. *Acta Crystallogr. D* **60,** 2126–2132
16. Murshudov, G. N., Vagin, A. A., and Dodson, E. J. (1997) Refinement of macromolecular structures by the maximum-likelihood method. *Acta Crystallogr. D* **53,** 240–255
17. Collaborative Computational Project, Number 4. (1994) The CCP4 suite: programs for protein crystallography. *Acta Crystallogr. D* **50,** 760–763
18. Afonine, P. V., Grosse-Kunstleve, R. W., Echols, N., Headd, J. J., Moriarty, N. W., Mustyakimov, M., Terwilliger, T. C., Urzhumtsev, A., Zwart, P. H., and Adams, P. D. (2012) Towards automated crystallographic structure refinement with phenix.refine. *Acta Crystallogr. D* **68,** 352–367
19. McCoy, A. J., Grosse-Kunstleve, R. W., Adams, P. D., Winn, M. D., Storoni, L. C., and Read, R. J. (2007) Phaser crystallographic software. *J. Appl. Crystallogr.* **40,** 658–674
20. Terwilliger, T. C., Adams, P. D., Read, R. J., McCoy, A. J., Moriarty, N. W., Grosse-Kunstleve, R. W., Afonine, P. V., Zwart, P. H., and Hung, L. W. (2009) Decision-making in structure solution using Bayesian estimates of map quality: the PHENIX AutoSol wizard. *Acta Crystallogr. D* **65,** 582–601
21. Terwilliger, T. C., Grosse-Kunstleve, R. W., Afonine, P. V., Moriarty, N. W., Zwart, P. H., Hung, L. W., Read, R. J., and Adams, P. D. (2008) Iterative model building, structure refinement and density modification with the PHENIX AutoBuild wizard. *Acta Crystallogr. D* **64,** 61–69
22. Kim, S. O., Yoon, H., Park, S. O., Lee, M., Shin, J. S., Ryu, K. S., Lee, J. O., Seo, Y. S., Jung, H. S., and Choi, B. S. (2012) Srs2 possesses a non-canonical PIP box in front of its SBM for precise recognition of SUMOylated PCNA. *J. Mol. Cell. Biol.* **4,** 258–261
23. Ludtke, S. J., Baldwin, P. R., and Chiu, W. (1999) EMAN: semiautomated software for high-resolution single-particle reconstructions. *J. Struct. Biol.* **128,** 82–97
24. Pettersen, E. F., Goddard, T. D., Huang, C. C., Couch, G. S., Greenblatt, D. M., Meng, E. C., and Ferrin, T. E. (2004) UCSF Chimera: a visualization system for exploratory research and analysis. *J. Comput. Chem.* **25,** 1605–1612
25. Wu, B., and Dong, D. (2012) Human cytosolic glutathione transferases: structure, function, and drug discovery. *Trends Pharmacol. Sci.* **33,** 656–668
26. Larkin, M. A., Blackshields, G., Brown, N. P., Chenna, R., McGettigan, P. A., McWilliam, H., Valentin, F., Wallace, I. M., Wilm, A., Lopez, R., Thompson, J. D., Gibson, T. J., and Higgins, D. G. (2007) ClustalW and ClustalX version 2. *Bioinformatics* **23,** 2947–2948
27. Rossjohn, J., McKinstry, W. J., Oakley, A. J., Verger, D., Flanagan, J., Chelvanayagam, G., Tan, K. L., Board, P. G., and Parker, M. W. (1998) Human θ class glutathione transferase: the crystal structure reveals a sulfate-binding pocket within a buried active site. *Structure* **6,** 309–322
28. Kim, K. J., Park, M. C., Choi, S. J., Oh, Y. S., Choi, E. C., Cho, H. J., Kim, M. H., Kim, S. H., Kim, D. W., Kim, S., and Kang B. S. (2008) Determination of three-dimensional structure and residues of the novel tumor suppressor AIMP3/p18 required for the interaction with ATM. *J. Biol. Chem.* **283,** 14032–14040
29. Crepin, T., Schmitt, E., Blanquet, S., and Mechulam, Y. (2004) Three-dimensional structure of methionyl-tRNA synthetase from *Pyrococcus abyssi*. *Biochemistry* **43,** 2635–2644
30. Nureki, O., O'Donoghue, P., Watanabe, N., Ohmori, A., Oshikane, H., Araiso, Y., Sheppard, K., Söll, D., and Ishitani, R. (2010) Structure of an archaeal non-discriminating glutamyl-tRNA synthetase: a missing link in the evolution of Gln-tRNAGln formation. *Nucleic Acids Res.* **38,** 7286–7297
31. Kwon, N. H., Kang, T., Lee, J. Y., Kim, H. H., Kim, H. R., Hong, J., Oh, Y. S., Han, J. M., Ku, M. J., Lee, S. Y., and Kim S. (2011) Dual role of methionyl-tRNA synthetase in the regulation of translation and tumor suppressor activity of aminoacyl-tRNA synthetase-interacting multifunctional protein-3. *Proc. Natl. Acad. Sci. U.S.A.* **108,** 19635–19640
32. Fu, Y., Kim, Y., Jin, K. S., Kim, H. S., Kim, J. H., Wang, D., Park, M., Jo, C. H., Kwon, N. H., Kim, D., Kim, M. H., Jeon, Y. H., Hwang, K. Y., Kim, S., and Cho, Y. (2014) Structure of the ArgRS-GlnRS-AIMP1 complex and its implications for mammalian translation. *Proc. Natl. Acad. Sci. U.S.A.* **111,** 15084–15089
33. Ahn, H. C., Kim, S., and Lee, B. J. (2003) Solution structure and p43 binding of the p38 leucine zipper motif: coiled-coil interactions mediate the association between p38 and p43. *FEBS Lett.* **542,** 119–124
34. Renault, L., Kerjan, P., Pasqualato, S., Ménétrey, J., Robinson, J. C., Kawaguchi, S., Vassylyev, D. G., Yokoyama, S., Mirande, M., and Cherfils, J. (2001) Structure of the EMAPII domain of human aminoacyl-tRNA synthetase complex reveals evolutionary dimer mimicry. *EMBO J.* **20,** 570–578
35. Ofir-Birin, Y., Fang, P., Bennett, S. P., Zhang, H. M., Wang, J., Rachmin, I., Shapiro, R., Song, J., Dagan, A., Pozo, J., Kim, S., Marshall, A. G., Schimmel, P., Yang, X. L., Nechushtan, H., Razin, E., and Guo, M. (2013) Structural switch of lysyl-tRNA synthetase between translation and transcription. *Mol. Cell* **49,** 30–42
36. Zhou, H., Sun, L., Yang, X. L., and Schimmel, P. (2013) ATP-directed

capture of bioactive herbal-based medicine on human tRNA synthetase. *Nature* **494,** 121–124
37. Kim, K. R., Park, S. H., Kim, H. S., Rhee, K. H., Kim, B. G., Kim, D. G., Park, M. S., Kim, H. J., Kim, S., and Han, B. W. (2013) Crystal structure of human cytosolic aspartyl-tRNA synthetase, a component of multi-tRNA synthetase complex. *Proteins* **81,** 1840–1846
38. Dias, J., Renault, L., Pérez, J., and Mirande, M. (2013) Small-angle X-ray solution scattering study of the multi-aminoacyl-tRNA synthetase complex reveals an elongated and multi-armed particle. *J. Biol. Chem.* **288,** 23979–23989
39. Negrutskii, B. S., Shalak, V. F., Kerjan, P., El'skaya, A. V., and Mirande, M. (1999) Functional interaction of mammalian valyl-tRNA synthetase with elongation factor: EF-1a in the complex with EF-1H. *J. Biol. Chem.* **274,** 4545–4550